International Journal of Solids and Structures 49 (2012) 701–719

Contents lists available at SciVerse ScienceDirect

International Journal of Solids and Structures

journal homepage: www.elsevier.com/locate/ijsolstr

# Performance Dependent Model for normal and high strength concretes

Paula Folino *, Guillermo Etse

*LMNI, INTECIN, FIUBA, Materials and Structures Laboratory, Faculty of Engineering, University of Buenos Aires, Argentina*

ARTICLE INFO

*Article history:*
Received 31 August 2011
Received in revised form 14 November 2011
Available online 9 December 2011

*Keywords:*
High strength concrete
Performance parameter
Constitutive formulation
Cap plasticity
Performance Dependent Failure Criterion

ABSTRACT

A new constitutive formulation, the so-called *Performance Dependent Model* valid for normal and high strength concretes is presented. The distinctive aspect of the proposed model is the consideration of relevant properties of concrete mix components in the evaluation of the involved material performance or quality at the macroscopic stand point. In this way, the composite features of concrete are appropriately taken into account.

The model maximum strength surface is defined by means of the *Performance Dependent Failure Criterion* proposed by the authors in previous works. Concrete behaviors in pre and post peak regimes are modeled with a non uniform hardening law and an isotropic softening rule, respectively. To realistically reproduce the concrete ductility in pre and post peak regimes under different load scenarios, the hardening and softening laws are defined in terms of the acting confining pressure. Concrete dilatancy behavior is approached by means of a volumetric non associative flow rule. The softening law is embedded in fracture energy concepts for mode I and II types of failure. The model considers two main input material parameters: the uniaxial compressive strength and the performance parameter, a quality index defined in the context of the Performance Dependent Failure Criterion.

The proposed constitutive model is able to capture the substantial differences in the failure behavior of normal and high strength concretes as well as of concretes with the same compressive strength but different mix components. The predictive capability of the model is demonstrated in the numerical analyses included in this paper where the numerical predictions are compared with experimental results related to concrete specimens of different qualities and subjected to stress histories under both compressive and tensile regimes.



## 1. Introduction

In recent years, there has been a significant growing trend to use concrete characterized with a superior performance to conventional, both in terms of their uniaxial compressive strength ($f'_c$) and of their elastic properties. This was aided by the need for greater slenderness in structures and the demands of higher strengths. From the concrete technology standpoint, the progress made during last decades is relevant. At present, concrete strengths of over 100 MPa can easily be achieved, what it is more than double the strength achieved in the early '90s.

In general terms, concrete presents a complex non linear behavior, characterized, among other features, by confinement sensitivity, inelastic dilatancy, softening, and path dependency. Its failure mode may vary from fragile in tensile regime, to quasi ductile in the low confinement regime and ductile in the high confinement one. On top of previous mentioned complexities, the experimental evidence demonstrates that failure behavior of normal strength concretes (NSC) substantially differs from that of high strength concretes (HSC), see e.g. van Mier (1997), Chen and Han (1988), Giaccio et al. (1993), Xie et al. (1995), Imran and Pantazopoulou (1996) and Rashid et al. (2002).

From the computational mechanics standpoint, substantial progress has been made in the modeling and simulation of failure behavior of conventional concrete. Much of this research was aimed at the macroscopic level of observation and based on the "smeared crack" concept, in which the post-peak strength decay of quasi-brittle materials like concrete is modeled through the stress–strain constitutive relation. Despite the advantages of the continuous approach from the numerical stand point, the strong mesh dependency of its computational predictions when localized failure modes are activated is a relevant shortcoming. To avoid or, moreover, to limit this effect, different enriched theories were proposed. This is the case of plasticity and damage-plasticity theories enriched with fracture mechanics, theories based on rate dependency, higher strain gradients, micropolar theory, etc. All of them invariably incorporate a characteristic length in the stress–strain relationship which is related to different properties of the involved structural problem, see e.g. Han and Chen (1987), Oller (1988), Pramono and Willam (1989), Dvorkin et al. (1989), Etse (1992), de

* Corresponding author. Tel./fax: +54 1145143009.
*E-mail address:* pfolino@fi.uba.ar (P. Folino).

0020-7683/$ - see front matter © 2011 Elsevier Ltd. All rights reserved.
doi:10.1016/j.ijsolstr.2011.11.020

Borst (1993), de Borst et al. (1993), Luccioni et al. (1996), Lee and Fenves (1998), Etse and Carosio (2002), Etse et al. (2003), Vrech and Etse (2009), etc. Nevertheless, most of the available concrete models were developed and calibrated for NSC. Therefore, their applicability to HSC may be questionable or would require complex calibration processes based on extensive experimental database. Some researchers have explicitly analyzed the case of HSC (see e.g. Imran and Pantazopoulou, 1996; Kang and Willam, 1999; Li and Ansari, 1999; Jason et al., 2006; Grassl and Jirásek, 2006; Vrech, 2007; Papanikolaou and Kappos, 2007). However, no existing proposal is able to capture within a unified approach the considerable differences in the failure behavior of concretes of arbitrary quality, covering the wide spectrum from NSC to HSC.

In this paper, a new concrete constitutive formulation, so-called *Performance Dependent Model* (PDM) is presented. The proposed model is valid for concretes with $f_c'$ from 20 to 120 MPa. The most relevant contribution of this macroscopic constitutive formulation is the inclusion of relevant aspects and features of the cement paste microstructure through the so-called *performance parameter* ($\beta_P$). In this way the PDM is capable to reproduce both the superior strength capabilities of HSC as well as the dramatic variations of the fracture energy properties and ductility with the involved material quality. It is also able to predict the variation in the mechanical behavior of concretes characterized by the same $f_c'$ but fabricated with different mix components. The constitutive formulation in this paper is based on the flow theory of plasticity. Its maximum strength surface is defined by the *Performance Dependent Failure Criterion for Concretes* (PDFC) (see Folino et al., 2009; Folino and Etse, 2011). It considers a non uniform hardening law and an isotropic softening rule. They are defined in terms of the concrete quality, through $\beta_P$, and of the acting confinement pressure to take into account its influence on the material ductility in both pre and post peak responses. A novel contribution in the hardening rule of the PDM is the inclusion of yield surfaces of cap-cone form with $C-1$ continuity. The cone portion is defined by the PDFC while the elliptical caps tangentially intersect the cone and are normal to the hydrostatic axis. In this way the numerical implementation of the model is considerably simplify, while pure hydrostatic loading paths are also allowed. The softening law is based on fracture energy concepts, leading to a variable internal characteristic length regarding the failure mode (type I or II) and the concrete quality. To limit excessive volumetric dilatancy in the low confinement regime, a volumetric non associative flow rule is considered which is also defined as a function of $\beta_P$ in order to reproduce the differences in the volumetric behaviors of NSC and HSC. After presenting the proposed constitutive theory for concretes of arbitrary strength based on the performance parameter, the paper focuses on its numerical predictions for different stress histories in tensile and compressive regimes and involving concretes qualities of a wide spectrum. The comparative analysis with experimental results demonstrates the predictive capabilities of the proposed model.

It should be also noted that the proposed material theory is suitable to be extended to a multiscale-type constitutive formulation based on microscopic calibrations of the performance parameter, which is the fundamental parameter of PDM. This can be done numerically with appropriate definition of the involved RVE to accurately evaluate the involved material quality by means of the performance parameter.

## 2. Mechanical behavior of NSC and HSC

The mechanical behavior of NSC and HSC shows some analogies but also fundamental differences. Due to the ongoing research process on experimental tests related to HSC, some aspects of the mechanical behavior of this particular material were so far not fully appreciated, understood, or moreover, discovered. Nevertheless clear conclusions regarding the relevant differences in the elastic properties, pre and post peak ductility, and the sensitivities to the confining pressure of both NSC and HSC can be obtained.

To start with the comparative evaluation of NSC and HSC mechanical behaviors, we evaluate in Fig. 1 the experimental results on uniaxial compression tests performed on concrete with different strength properties. (Data extracted from Hurlbut (1985), van Geel (1998), Lu (2005), and Xie et al. (1995).) In this figure, it can be appreciated that the elastic stiffness tends to increase with the material strength properties in the initial regime of the pre-peak or hardening response. This indicates that the elastic stiffness of concrete mixture is very much dependent on the mortar elastic properties, when normal or standards contents of coarse aggregate are considered.

From the comparison between mechanical behaviors in the uniaxial compression tests shown in Fig. 1 follows also that the ductility in post peak regime varies with the involved material quality. In this sense, it can be observed a reduction of the deformation capability in softening with increments of the involved concrete strength capability. To demonstrate this, Fig. 2 shows the dependence of the ductility factor in softening, evaluated as the ratio between the axial strain in softening at 50% $f_c'$ and the strain at peak, with $f_c'$. The decrement of the ductility factor in softening with the strength capability of concrete is clear.

Based on the evaluation of many experimental results on concretes of different strength properties, Lee (2002) proposed an empirical equation to predict the uniaxial stress–strain response of HSC of different strength qualities in the uniaxial compression test. The prediction of this equation for different strength properties are illustrated in Fig. 3 where the differences in the mechanical behavior of NSC and HSC can be identifies, based on the evaluations by Lee (2002) for HSC and by Carreira and Chu (1985) for NSC. One fundamental difference is the elastic stiffness. According to Lee, the increment of concrete elastic stiffness in the pre-peak

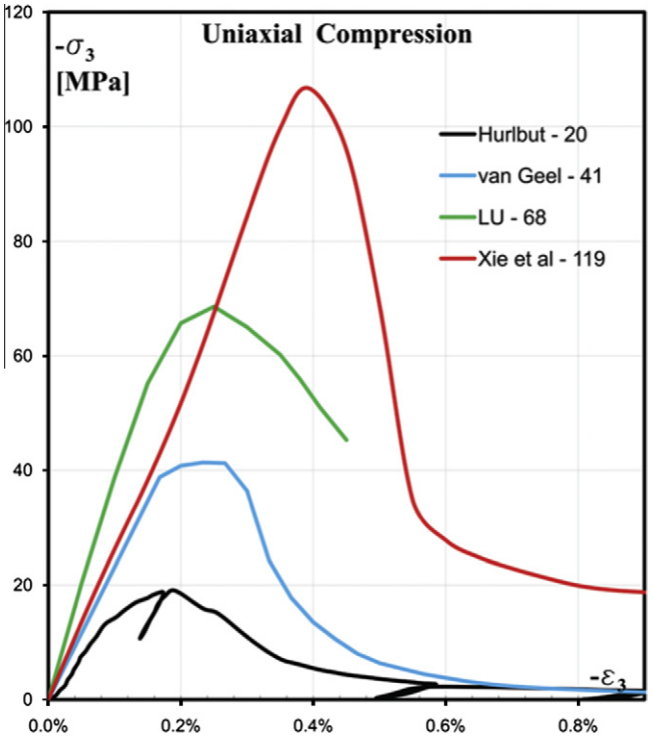


**Fig. 1.** Uniaxial compression – experimental results for different concrete strengths.

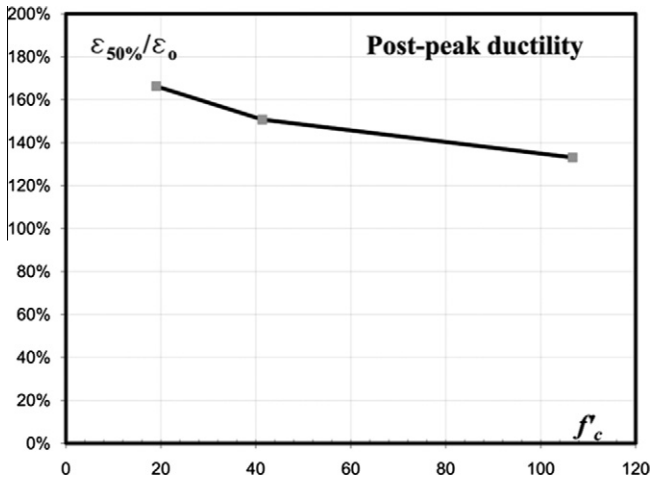


**Fig. 2.** Uniaxial compression – ductility factor in softening vs. $f'_c$.

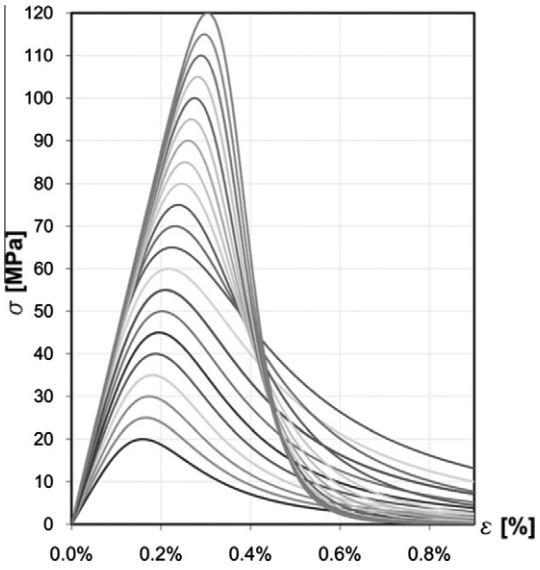


**Fig. 3.** Empirical uniaxial compression curves for different concretes.

regime may be considered linear and almost continuous with the increment of the involved concrete strength. Experimental results in the literature (see a.o. Rashid et al., 2002; Giaccio et al., 1992) demonstrate that Young's Modulus is much more dependent on the type and geometry of the coarse aggregates than on the compressive strength of concrete.

When subjected to confining pressure, both NSC and HSC show important increment of strength and ductility. Fig. 4(a) and (b) illustrate the results of triaxial compression tests under different levels of lateral confinements performed on 68 MPa and 119 MPa concretes, respectively. (Data extracted from Lu (2005) and Xie et al. (1995).) As can be observed in these figures, both curve series show the increments of strength and ductility in pre and post-peak regimes. Moreover, it can be observed that the elastic stiffness in the initial loading process remains constant and practically does not depend on the acting confinement. One relevant aspect is that the sensitivity of the strain at peak strength on the acting confinement decreases with the involved concrete quality. This can be concluded from the comparison between the ratios of axial strains at peak of the triaxial tests with $\sigma_{conf} = 0.41\ f'_c$ and $\sigma_{conf} = 0$ of the $f'_c = 68$ MPa concrete, on the one hand, and of the tests corresponding to $\sigma_{conf} = 0.40\ f'_c$ and $\sigma_{conf} = 0$ of the $f'_c = 119$ MPa concrete, on the other hand. These ratios are 9.33 and 4.25 in case of the $f'_c = 68$ MPa and $f'_c = 119$ MPa concretes. With other words, the ductility at peak strength is much more sensitive to the confinement level in NSC than HSC.

From the last figures corresponding to triaxial compression tests on $f'_c = 68$ MPa and $f'_c = 119$ MPa concretes can also be concluded that stress decay after peak increases with the involved concrete quality.

Considering the major sensitivity of the axial strain on the acting confinement observed in case of the NSC, it can be assumed that the same conclusion can be obtained regarding the lateral strains. Thus, the kinematic fields of NSC are more sensitive to the confinement pressure than those of HSC.

Regarding the tensile strength $f'_t$ variation with the considered concrete quality (see Fig. 5 – data extracted from Navalurkar (1996) and Li and Ansari (2000)), the analysis of several experimental results demonstrates that the ratio $\alpha_t = f'_t/f'_c$ (normalized uniaxial tensile strength), although having a linear variation at low values of $f'_c$, it turns not linear once $f'_c$ equals the values of medium strength concretes. From this level of concrete quality, the experimental evidence demonstrates that the increase of $f'_t$ is very small as compared to that of $f'_c$. Consequently, the maximum strength normalized surfaces of concretes of arbitrary quality would show practically no expansion of the tensile meridian when varying from medium to high strength concretes. However, the compressive meridians would show clear expansions. These features were considered in the formulation of maximum strength surface for concretes of arbitrary quality by Folino et al. (2009) and Folino and Etse (2011).

In Fig. 6 can be observed deviatoric views of the maximum strength criteria for NSC and HSC proposed by Folino et al. (2009). In case of HSC these plots are less rounded than those of NSC due to the lower normalized uniaxial tensile strength involved.

Usually, the quality of a concrete is identified by $f'_c$. Nevertheless, different concrete mixtures may lead to the same value of $f'_c$. This fact motivated the authors to define an additional quality index in order to objectively quantify the material quality. Hence, after an extensive parametric analysis, $\beta_P$, the performance parameter for concretes was defined as (see Folino et al., 2009)

$$\beta_P = \frac{1}{1000}\frac{f'_c}{(w/b)} \quad [\text{with } f'_c \text{ in MPa}] \tag{1}$$

where $w/b$ is the water-binder ratio, being $W$ the water content and $B$ the binder content, both in [kg/m$^3$]. The binder is constituted by the sum of the cement and the mineral admixtures contents. Conceptually, the performance parameter reflects the different levels of homogeneity of different concretes as it may be appreciated in Fig. 7. In the case of NSC, the coarse aggregates are much more rigid than the cement paste and the porosity is greater than the corresponding to HSC. While increasing the concrete quality, the composite material will be more homogeneous and less porous. Ideally $\beta_P$ varies from 0 to 1.

It was demonstrated based on experimental results that for a given $f'_c$ value, the performance parameter lies between a minimum and a maximum value. Then, the following approximation curves were proposed for those limits which are plot in Fig. 8

$$\beta_{P\max} = \begin{cases} 0.00026 \cdot (f'_c + 5)^{1.60} & \text{when } f'_c \leqslant 55 \text{ MPa} \\ 0.04 \cdot e^{(0.025 \cdot (f'_c + 5))} & \text{when } f'_c > 55 \text{ MPa} \end{cases} \tag{2}$$

$$\beta_{P\min} = \begin{cases} 0.00026 \cdot (f'_c - 5)^{1.60} & \text{when } f'_c \leqslant 55 \text{ MPa} \\ 0.04 \cdot e^{(0.025 \cdot (f'_c - 5))} & \text{when } f'_c > 55 \text{ MPa} \end{cases} \tag{3}$$

If the $w/b$ ratio is unknown, these approximation limiting curves permit to select a medium value for $\beta_P$ and moreover, to know the whole range of possible $\beta_P$ that corresponds to the target $f'_c$.

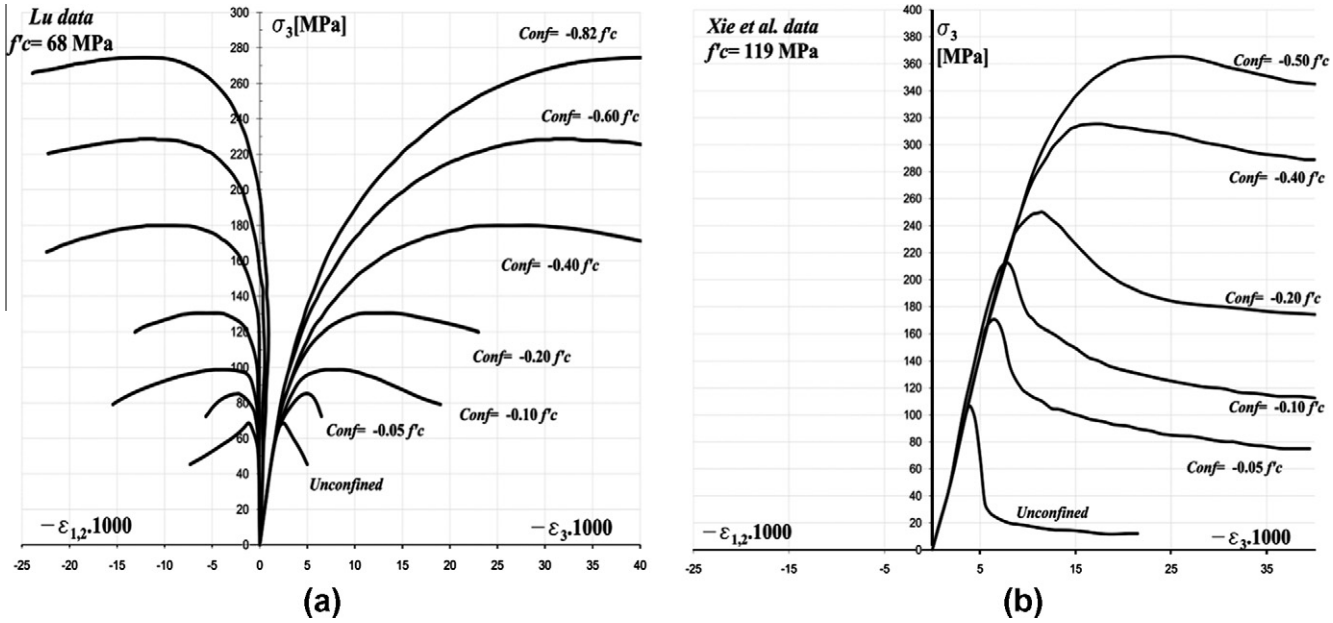


**Fig. 4.** Triaxial compression – experimental results (a) $f_c'' = 68$ MPa and (b) $f_c'' = 119$ MPa.

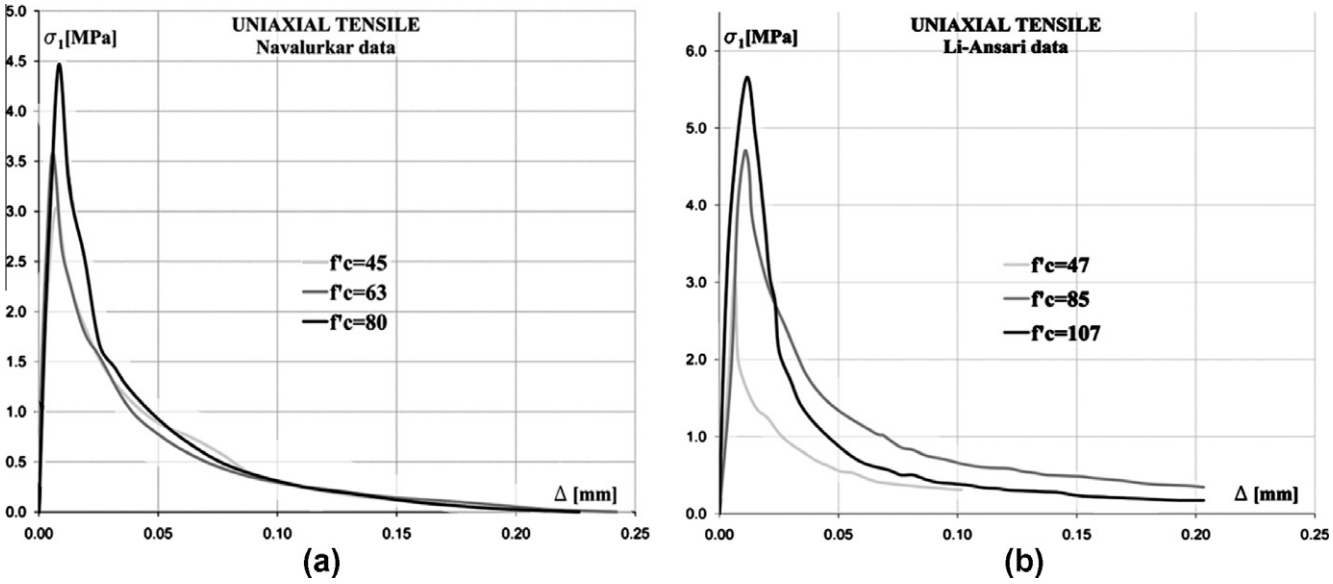


**Fig. 5.** Uniaxial tensile – experimental results (a) $f_c'' = 45, 63, 80$ MPa and (b) $f_c'' = 47, 85, 107$ MPa.

## 3. Performance dependent constitutive model for concretes of arbitrary strength : main equations

Regarding that for concretes the current stresses state depends on the current strains as well as on the stress path followed to reach this state, an incremental constitutive formulation is proposed. The elastoplastic incremental non-associative flow theory and the smeared crack approach are adopted as theoretical frame. In order to describe the post peak behavior of concrete, fracture energy concepts are considered, leading to a non local elastoplastic formulation.

Only infinitesimal strains are admitted. Elastic–plastic coupling is neglected, accepting the additive Prandtl–Reuss decomposition of the infinitesimal strain rate tensor into its elastic and plastic parts. Denoting the time derivative as an upper dot, and using the superscripts "*E*" and "*P*" to identify the elastic and plastic contributions

$$\dot{\underline{\underline{\varepsilon}}} = \dot{\underline{\underline{\varepsilon}}}^E + \dot{\underline{\underline{\varepsilon}}}^P \tag{4}$$

The elastic constitutive response is defined by the generalized Hooke law

$$\dot{\underline{\underline{\varepsilon}}}^E = \underline{\underline{\underline{\underline{\boldsymbol{E}}}}}^{-1} : \dot{\underline{\underline{\boldsymbol{\sigma}}}} \tag{5}$$

In the above equation $\dot{\underline{\underline{\boldsymbol{\sigma}}}}$ is the Cauchy stress rate tensor, $\underline{\underline{\underline{\underline{\boldsymbol{E}}}}}$ is the fourth order elasticity tensor depending on the material Young's modulus $E$ and on the Poisson's ratio $\nu$. A yield surface denoted as $f$, limits the elastic range, which size and shape depend on a set of state variables $q$. Inelastic material response is governed, by the following non associated flow rule

$$\dot{\underline{\underline{\varepsilon}}}^P = \underline{\underline{\boldsymbol{m}}}\dot{\lambda} \tag{6}$$

where

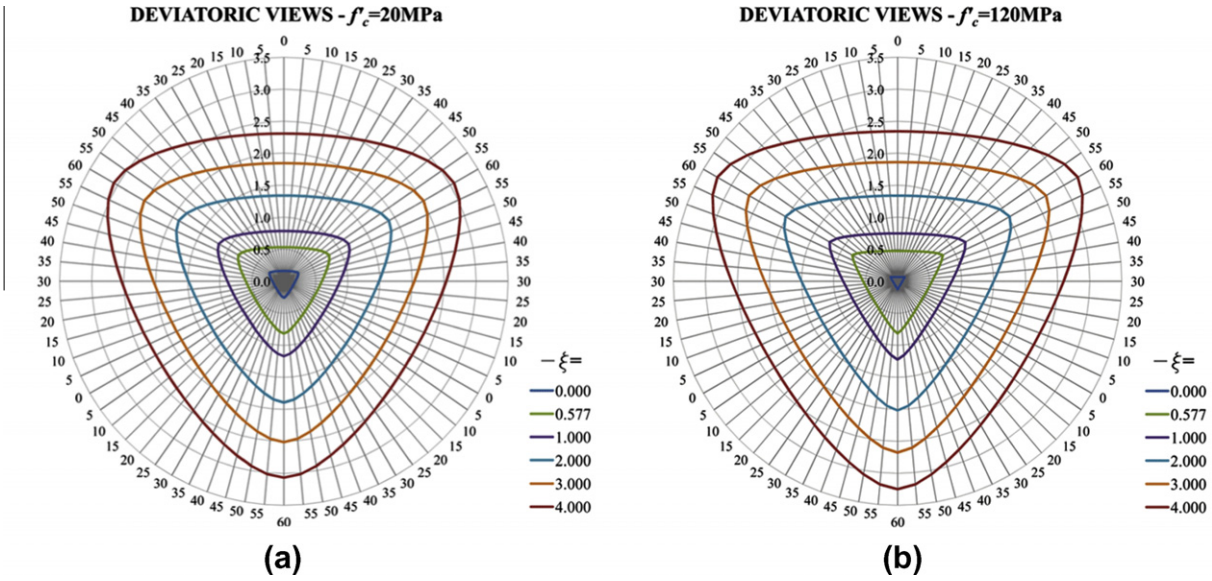


**Fig. 6.** Deviatoric views for (a) NSC and (b) HSC.

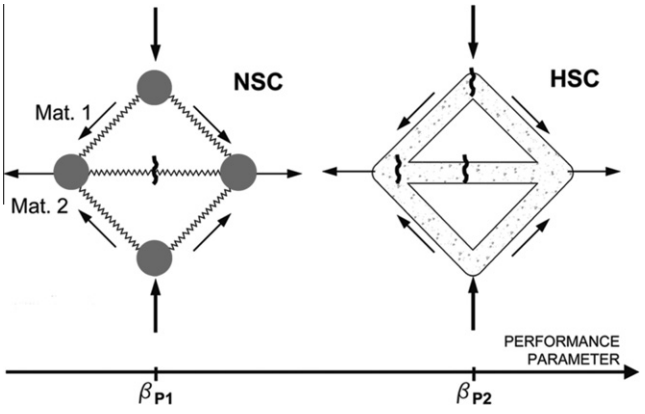


**Fig. 7.** The concept of the performance parameter $\beta_P$.

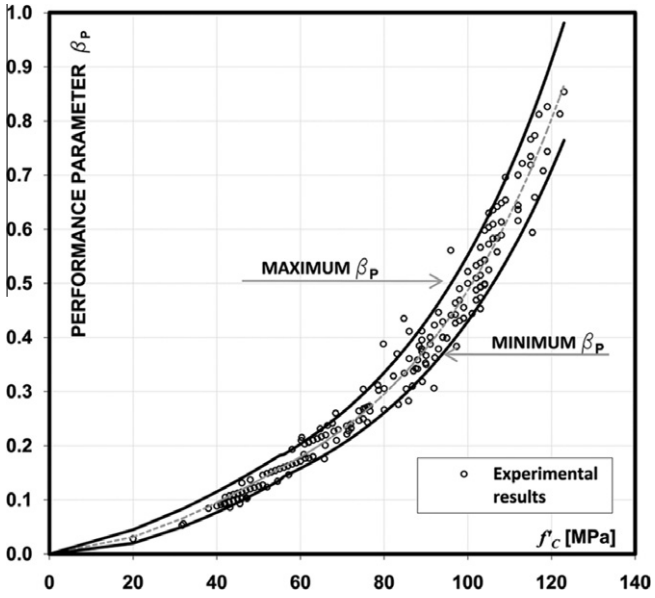


**Fig. 8.** $f'_c$ vs. $\beta_P$ – minimum and maximum limiting curves proposed.

$$\underline{\underline{\boldsymbol{m}}} = \frac{\partial g}{\partial \underline{\underline{\boldsymbol{\sigma}}}} \tag{7}$$

Being $g$ the plastic potential surface, which does not coincide with the yield surface $f$, and $\dot{\lambda}$ the plastic parameter (or plastic multiplier), a nonnegative function which is assumed to obey the following Kuhn–Tucker complementary conditions of optimization theory

$$\dot{\lambda} \geqslant 0; \quad f \leqslant 0; \quad \dot{\lambda} f = 0 \tag{8}$$

Eqs. (4)–(6) lead to the following subtractive decomposition of the total stress rates

$$\dot{\underline{\underline{\boldsymbol{\sigma}}}} = \underline{\underline{\underline{\underline{\boldsymbol{E}}}}} : (\dot{\underline{\underline{\boldsymbol{\varepsilon}}}} - \underline{\underline{\boldsymbol{m}}}\dot{\lambda}) \Rightarrow \dot{\underline{\underline{\boldsymbol{\sigma}}}} = \dot{\underline{\underline{\boldsymbol{\sigma}}}}^E - \dot{\underline{\underline{\boldsymbol{\sigma}}}}^P \tag{9}$$

As a consequence of the fulfillment of the third Kuhn–Tucker condition, it follows the so-called consistency condition

$$\dot{f} = \underline{\underline{\boldsymbol{n}}} : \dot{\underline{\underline{\boldsymbol{\sigma}}}} + \partial f_q \dot{q} = 0 \tag{10}$$

where

$$\underline{\underline{\mathbf{n}}} = \frac{\partial f}{\partial \underline{\underline{\boldsymbol{\sigma}}}} \quad \text{and} \quad \partial f_q = \frac{\partial f}{\partial q} \tag{11}$$

The evolution of the state variables $\dot{q}$ is defined by the hardening/softening laws.

$$\dot{q} = \underline{\underline{\boldsymbol{h}}} : \dot{\underline{\underline{\boldsymbol{\varepsilon}}}}^P \quad \text{with} \quad \underline{\underline{\boldsymbol{h}}} = \frac{\partial q}{\partial \underline{\underline{\boldsymbol{\varepsilon}}}^P} \tag{12}$$

Defining the *hardening tensor* $\underline{\underline{\boldsymbol{H}}}$ as

$$\underline{\underline{\boldsymbol{H}}} = -\frac{\partial f}{\partial \underline{\underline{\boldsymbol{\varepsilon}}}^P} = -\frac{\partial f}{\partial q}\frac{\partial q}{\partial \underline{\underline{\boldsymbol{\varepsilon}}}^P} = -\partial f_q \underline{\underline{\boldsymbol{h}}} \tag{13}$$

then the plastic multiplier may be derived from the consistency condition as follows

$$\dot{f} = \underline{\underline{\boldsymbol{n}}} : \dot{\underline{\underline{\boldsymbol{\sigma}}}} - \underline{\underline{\boldsymbol{H}}} : \underline{\underline{\boldsymbol{m}}}\dot{\lambda} = \underline{\underline{\boldsymbol{n}}} : \underline{\underline{\underline{\underline{\boldsymbol{E}}}}} : \left(\dot{\underline{\underline{\boldsymbol{\varepsilon}}}} - \underline{\underline{\boldsymbol{m}}}\dot{\lambda}\right) - \underline{\underline{\boldsymbol{H}}} : \underline{\underline{\boldsymbol{m}}}\dot{\lambda} = 0 \tag{14}$$

$$\Rightarrow \dot{\lambda} = \frac{\underline{\underline{\boldsymbol{n}}} : \underline{\underline{\underline{\underline{\boldsymbol{E}}}}}}{\underline{\underline{\boldsymbol{n}}} : \underline{\underline{\underline{\underline{\boldsymbol{E}}}}} : \underline{\underline{\boldsymbol{m}}} + \underline{\underline{\boldsymbol{H}}} : \underline{\underline{\boldsymbol{m}}}} : \dot{\underline{\underline{\boldsymbol{\varepsilon}}}} \tag{15}$$

The scalar magnitude resulting from the double contraction of the tensors $\underline{\underline{\boldsymbol{H}}}$ and $\underline{\underline{\boldsymbol{m}}}$ is known as hardening modulus $h_p$

$$h_p = \underline{\underline{\boldsymbol{H}}} : \underline{\underline{\boldsymbol{m}}} \tag{15}$$

Then, by defining the material elastoplastic operator as

$$\underline{\underline{\underline{\underline{\boldsymbol{E}}}}}^{EP} = \underline{\underline{\underline{\underline{\boldsymbol{E}}}}} - \frac{\underline{\underline{\underline{\underline{\boldsymbol{E}}}}} : \underline{\underline{\boldsymbol{m}}}\ \underline{\underline{\boldsymbol{n}}} : \underline{\underline{\underline{\underline{\boldsymbol{E}}}}}}{\underline{\underline{\boldsymbol{n}}} : \underline{\underline{\underline{\underline{\boldsymbol{E}}}}} : \underline{\underline{\boldsymbol{m}}} + \underline{\underline{\boldsymbol{H}}} : \underline{\underline{\boldsymbol{m}}}} \tag{16}$$

the constitutive relation takes the final form

$$\dot{\underline{\underline{\boldsymbol{\sigma}}}} = \underline{\underline{\underline{\underline{\boldsymbol{E}}}}}^{EP} : \dot{\underline{\underline{\boldsymbol{\varepsilon}}}} \tag{17}$$

Considering that a non associative flow rule is followed, the elastoplastic operator is non-symmetric. Nevertheless, it preserves the minor symmetries $\left(E^{EP}_{ijkl} = E^{EP}_{jikl} = E^{EP}_{ijlk} = E^{EP}_{jilk}\right)$.

## 4. Maximum strength criterion for concretes of arbitrary strength

The maximum strength surface is defined by the Performance Dependent Failure Criterion (PDFC) for concretes of arbitrary strength which is briefly described in this section. For further details, see Folino et al. (2009). This criterion, covering the entire spectrum of concrete quality from NSC to HSC, is defined in the Haigh Westergaard stress space in terms of the normalized stress coordinates (with respect to $f'_c$) $\bar{\xi}$, $\bar{\rho}$ and $\theta$, depending therefore on the three stress invariants $I_1, J_2$ and $J_3$. These normalized coordinates are defined as

$$\bar{\xi} = \frac{\xi}{f'_c} = \frac{I_1}{\sqrt{3} f'_c}; \quad \bar{\rho} = \frac{\rho}{f'_c} = \frac{\sqrt{2J_2}}{f'_c}; \quad \cos(3\theta) = \frac{3\sqrt{3}}{2}\frac{J_3}{J_2^{3/2}} \tag{18}$$

where: $I_1 = \delta_{ij}\sigma_{ij}$ is the first invariant of the stress tensor $\underline{\underline{\boldsymbol{\sigma}}}$; $J_2 = s_{ij}s_{ij}/2$ the second invariant of the deviatoric stress tensor $\underline{\underline{\boldsymbol{s}}}$; and $J_3 = s_{ij}s_{jk}s_{ki}/3$ the third invariant of the deviatoric stress tensor.

Concrete failure occurs when the normalized 2nd Haigh Westergaard stress coordinate reaches the normalized shear strength

$$F_{max} = \frac{\bar{\rho}}{\bar{\rho}^*} - 1 = 0 \tag{19}$$

The compressive and tensile meridians are defined by two parabolic equations

$$\theta = \frac{\pi}{3} \Rightarrow A\overline{\rho^*_c}^2 + B_c\overline{\rho^*_c} + C\bar{\xi} - 1 = 0 \tag{20}$$

$$\theta = 0 \Rightarrow A\overline{\rho^*_t}^2 + B_t\overline{\rho^*_t} + C\bar{\xi} - 1 = 0 \tag{21}$$

In the previous equations, the upper asterisk denotes failure, the subscripts "c" and "t" indicate compressive and tensile meridians respectively.

In the deviatoric plane, the elliptic interpolation between the compressive and tensile meridians by Willam and Warnke (1974) is considered as

$$\forall 0^0 \leqslant \theta \leqslant 60^0 \Rightarrow \overline{\rho^*} = \frac{\overline{\rho^*_c}}{r} \tag{22}$$

The ellipticity factor $r$ is defined as

$$r = \frac{4(1-e^2)\cos^2\theta + (2e-1)^2}{2(1-e^2)\cos\theta + (2e-1)\sqrt{4(1-e^2)\cos^2\theta + 5e^2 - 4e}} \tag{23}$$

where $e$ is the eccentricity $\overline{\rho^*_t}/\overline{\rho^*_c}$.

Consequently the above expressions lead to the following single equation representing the failure criterion of concretes of arbitrary strength

$$F_{max} = Ar^2\overline{\rho^*}^2 + B_c r\overline{\rho^*} + C\bar{\xi} - 1 = 0 \tag{24}$$

A distinguish characteristic of the criterion in Eq. (24) is that the coefficients $A$, $B_c$, $B_t$, and $C$ instead of being simple constants are defined in terms of four relevant material features: the uniaxial compression strength $f'_c$, the normalized uniaxial tensile strength $\alpha_t = f'_t/f'_c$, the normalized biaxial compression strength $\alpha_b = f'_b/f'_c$ (being $f'_b$ the biaxial compressive strength), and the apparent friction $m$ defined as the tangent to the compressive meridian on the peak stress state corresponding to the uniaxial compression test. Thus, the coefficients in Eq. (24) are defined in terms of real material properties that allow accurate descriptions of maximum strength surfaces of concrete of different qualities.

As the material properties $\alpha_t$, $\alpha_b$ and $m$ are obtained from non-standard and complex experimental tests, internal functions were proposed and calibrated to determine them in terms of only two fundamental concrete parameters: $f'_c$ and $\beta_P$ (see Folino and Etse, 2011).

The equations defining coefficients $A$, $B_c$, $B_t$, and $C$ in terms of the material properties $\alpha_t$, $\alpha_b$ and $m$, and the equation corresponding to the eccentricity $e$, are given in Appendix A.

## 5. Hardening for concretes of arbitrary strength

### 5.1. Loading surfaces in pre peak regime

In most of the available constitutive models for concrete, open loading surfaces are considered to predict the variation of stiffness in hardening, see e.a. Oller (1988), Grassl et al. (2002) and Papanikolaou and Kappos (2007). In those models the elastic zone does not have a limit on the negative side of the hydrostatic pressure axis. This is not in agreement with experimental evidence as plastic behavior is observed in pure hydrostatic loading, see Oller (1988) and Sfer et al. (2002). Although some proposals do consider close loading surfaces like the ones by Han and Chen (1987), and Fossum and Fredrich (2000) they are $C^o$ continuum curves. So, their numerical treatments are particularly complex. In other proposals such as the one by Etse and Willam (1994) the yield surfaces in hardening, although close and $C^1$ continuum, are obtained by means of very high order functions of the stress invariants that, on top of this, do not intersect perpendicularly the hydrostatic axis in the high compressive regime.

In the constitutive model here proposed, the loading surfaces in hardening are of cap-cone type and have three relevant advantages: (i) they are of $C^1$ continuity, (ii) they are of second order and (iii) they perpendicularly intersect the hydrostatic axis in compression. As it can be observed in Fig. 9, the meridian view of the proposed yield surfaces provides a continuum $C^1$ transition from the conic failure surface on the tensile and low confinement regimes to the cap portion on the medium and high confinement regimes. The cap is defined by elliptical meridians centered on the hydrostatic axis. Both portions of the yield surfaces, the cap and the cone, intersect each other at a deviatoric plane indicated with the stress point "P1" in the meridian view of Fig. 11. During monotonic loading in hardening regime the location of the stress point "P1" on the maximum strength criterion moves to the compressive regime, see Fig. 10. As its typically the case of cap-cone loading surfaces, loading paths approaching the maximum strength surface between "P1" and the stress point corresponding to the equitriaxial tensile loading, do not activate hardening behavior, i.e. the maximum strength point is reached without degradation of the elastic properties. Since point "P1" lies on the maximum strength surface, its coordinates on the compressive meridian $(\bar{\xi}_1; \bar{\rho}_{c1})$ follow from Eq. (20)

$$\bar{\xi}_1 = \left(1 - Ay_1^2 - B_c y_1\right)/C \quad \text{with} \quad y_1 = \bar{\rho}_{c1} \tag{25}$$

The evolution of the loading surfaces in pre-peak regime are controlled by the hardening parameter $k$ defined in terms of the $\bar{\rho}_{c1}$ coordinate of point "P1" as

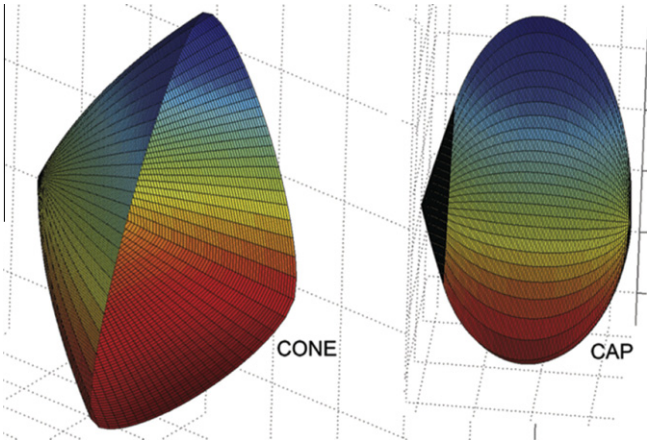


**Fig. 9.** 3-D view of the failure surface (cone) and of an intermediate loading surface (cap-cone).

$$k = \frac{\bar{\rho}_{c1}}{\sqrt{2/3}} \tag{26}$$

This parameter has a minimum initial value $k_o$ corresponding to the first loading surface where the inelastic behavior starts (see Appendix A). However, it has no upper limit, as the hardening ductility may evolve indefinitely under increasing confining pressure.

The yield surfaces in hardening regime of the proposed model are defined as follows

$$f_h = \begin{cases} f_h^{cone} = F_{max} = Ar^2\overline{\rho*}^2 + B_c r\overline{\rho*} + C\bar{\xi} - 1 = 0 & \text{if } \bar{\xi} \geqslant \bar{\xi}_{1(k)} \\ f_{h(k)}^{cap} = \frac{\left(\bar{\xi}-\bar{\xi}_{cen(k)}\right)^2}{a_{(k)}^2} + \frac{r^2\bar{\rho}^2}{b_{(k)}^2} - 1 = 0 & \text{if } \bar{\xi} < \bar{\xi}_{1(k)} \end{cases} \tag{27}$$

being $a$ and $b$ the semi axes of the elliptical cap on the hydrostatic and deviatoric axes, and $\bar{\xi}_{cen}$ the normalized first stress coordinate of the elliptical cap center. The evolution laws of these coefficients of the elliptical cap are controlled by the hardening parameter $k$.

Appendix A includes details about how the first ellipse and the successive ellipses are obtained. The final functions of the parameters that define the shape of the caps surfaces are as follows

$$\bar{\xi}_{cen(k)} = \frac{1}{C}\left[1 - A\frac{2}{3}k^2 - B_c\sqrt{\frac{2}{3}}k - \sqrt{\frac{2}{3}}\frac{C^2R_{ab}}{2Ak\sqrt{2/3}+B_c}k\right] \tag{28}$$

$$a_{(k)}^2 = \left[\frac{1}{C}\left(1 - \frac{2}{3}Ak^2 - \sqrt{\frac{2}{3}}B_c k\right) - \bar{\xi}_{cen(k)}\right]^2 + \frac{2}{3}R_{ab}k^2 \tag{29}$$

$$b_{(k)}^2 = a_{(k)}^2/R_{ab} \tag{30}$$

After replacing Eqs. (28)–(30) in Eq. (27), the following polynomial form of the caps in terms of the hardening parameter $k$ is obtained

$$\begin{aligned} f_{h(k)}^{cap} = {} & \left\{\left[\frac{8}{9}A^3\right]k^5 + \left[\frac{10}{3}\sqrt{\frac{2}{3}}A^2B_c\right]k^4 + \left[\frac{8}{3}A\left(A(C\bar{\xi}-1)+B_c^2\right)\right]k^3 \right. \\ & + \left[\sqrt{\frac{2}{3}}B_c\left(6A(C\bar{\xi}-1)+B_c^2+C^2R_{ab}\right)\right]k^2 \\ & + \left[2\left[\left(B_c^2+C^2R_{ab}\right)(C\bar{\xi}-1)+A(C\bar{\xi}(C\bar{\xi}-2)+1C^2R_{ab}r^2\bar{\rho}^2)\right]\right]k \\ & \left. + \left[\sqrt{\frac{3}{2}}B_c\left(C\bar{\xi}(C\bar{\xi}-2)+1+C^2R_{ab}r^2\bar{\rho}^2\right)\right] = 0 \end{aligned} \tag{31}$$

### 5.2. Hardening law

Following Etse and Willam (1994) the hardening parameter in this model is defined by means of an elliptical function, which in this case depends on a normalized work hardening measure $\kappa_h$ as

$$k = k_o + (k_{max} - k_o)\sqrt{\kappa_h(2-\kappa_h)} \tag{32}$$

being $k_{max}$ the maximum possible hardening parameter associated with the actual confinement level $\bar{\xi}$. It is obtained by replacing Eq. (26) in (20), leading to

$$k_{max} = \frac{1}{\sqrt{2/3}}\frac{-B_c + \sqrt{B_c^2 + 4A(1-C\bar{\xi})}}{2A} \tag{33}$$

It should be noted that while the minimum hardening parameter $k = k_o$ is defined, the maximum value of $k = k_{max}$ is not. It could be lower or greater than one. In Fig. 12 it can be observed that the evolution of the ratio $k/k_{max}$ reduces its intensity with increment of the acting confinement. Comparing NSC and HSC, it may be seen that in case of HSC the inelastic range in pre-peak regime is shorter for every considered confinement level.

The evolution law of the normalized work hardening measure is defined as the ratio between the actual developed work hardening

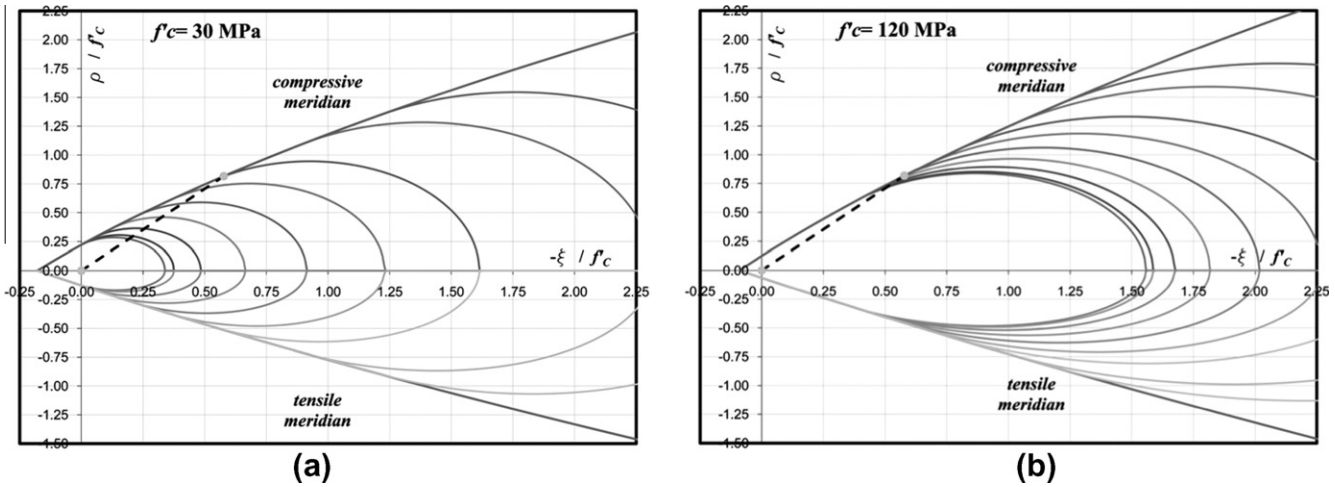


**Fig. 10.** Compressive and tensile meridian views of the loading surfaces in hardening for (a) NSC and (b) HSC.

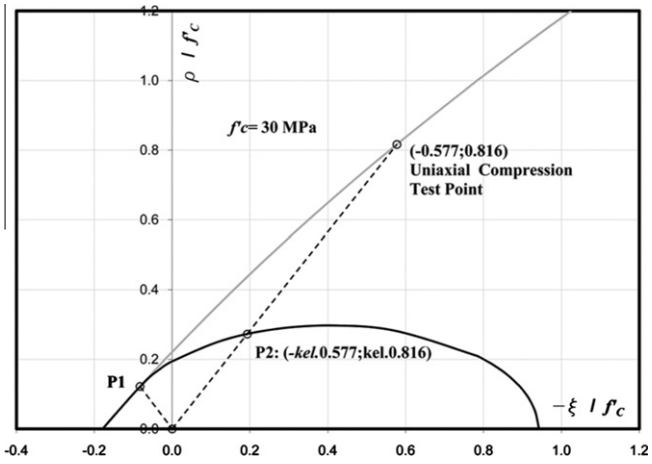


**Fig. 11.** Compressive meridian view of the first loading surface in hardening.

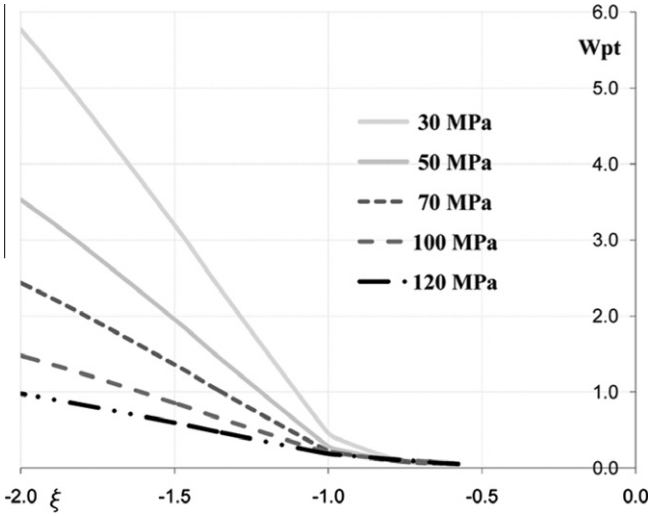


**Fig. 13.** Calibration adopted for the pre peak energy parameter $W_t^p$.

$\omega_a^p$, and the total work hardening capacity $W_t^p$ for the actual confinement level $\bar{\xi}$

$$\dot{\kappa}_h = \frac{\dot{\omega}_a^p}{W_t^p} = \frac{\underline{\underline{\boldsymbol{\sigma}}} : \underline{\underline{\boldsymbol{m}}}\dot{\lambda}}{W_t^p} \tag{34}$$

The total plastic work capacity in hardening $W_t^p$ is approximated by means of the following function

$$W_t^p \begin{cases} = E^{wpt}_{(\beta_p, f'_c)}\left(\bar{\xi} - \bar{\xi}_{P1o}\right)\left[f_1 + f_2\left(\bar{\xi} - \bar{\xi}_{P1o}\right)^6\right] & \text{if } \bar{\xi} \geqslant \bar{\xi}_{lim} \\ = f_3\bar{\xi}^2 + f_4\bar{\xi} + f_5 & \text{if } \bar{\xi} < \bar{\xi}_{lim} \end{cases} \tag{35}$$

where $f_i$, $\bar{\xi}_{lim}$ and $E_{wpto}$ are defined in terms of the performance parameter $\beta_P$. Thus, it is considered that the total plastic work capacity in hardening depends on both the involved material quality and the level of confinement. Fig. 13 shows the dependence of $W_t^p$ on the acting confinement for different concrete qualities.

## 6. Softening for concretes of arbitrary strength

### 6.1. Unloading surfaces in post peak regime

Once the maximum strength surface was reached and under continuous monotonic loading, the softening law of the model is activated. In this formulation, an isotropic softening law is adopted. The plastic yield surfaces in post-peak regime are obtained by progressive contraction of the cone portion of the maximum strength surface. This progressive degradation of the concrete strength properties is controlled by a decohesion process of the concrete matrix, that is defined in the model through the softening of the cohesion $c$. It is considered that this parameter represents the ratio between the actual and the maximum strength property both under mode I and II type of softening processes. Consequently, it varies between a maximum value $c = 1$ at peak strength, before activating the degradation or softening process in the material, and a minimum value $c = \sigma_{res}/\sigma_{max}$, being $\sigma_{res}$ the residual strength and $\sigma_{max}$, the maximum one. In case of mode I type of failure process results $\sigma_{max} = f'_t$ and the actual strength is represented by $\sigma_t$.

The unloading surfaces in post-peak regime are mathematically described by (see Fig. 14)

$$f_s = Ar^2\bar{\rho}^2 + B_c r\bar{\rho} + C\bar{\xi} - c = 0 \tag{36}$$

In this formulation it is considered that the softening behavior develops for all possible monotonic loading process after the peak stress was reached. This softening behavior is activated independently of the confinement level in the considered stress history. However, the ductility of the post-peak response varies with the level of confinement as is explained in this section. The experimental evidence demonstrates that in HSC the softening branch develops for all possible level of confinement. However, in case of NSC a transition point from brittle to ductile behavior can be recognized that delimits the region of the stress space where softening

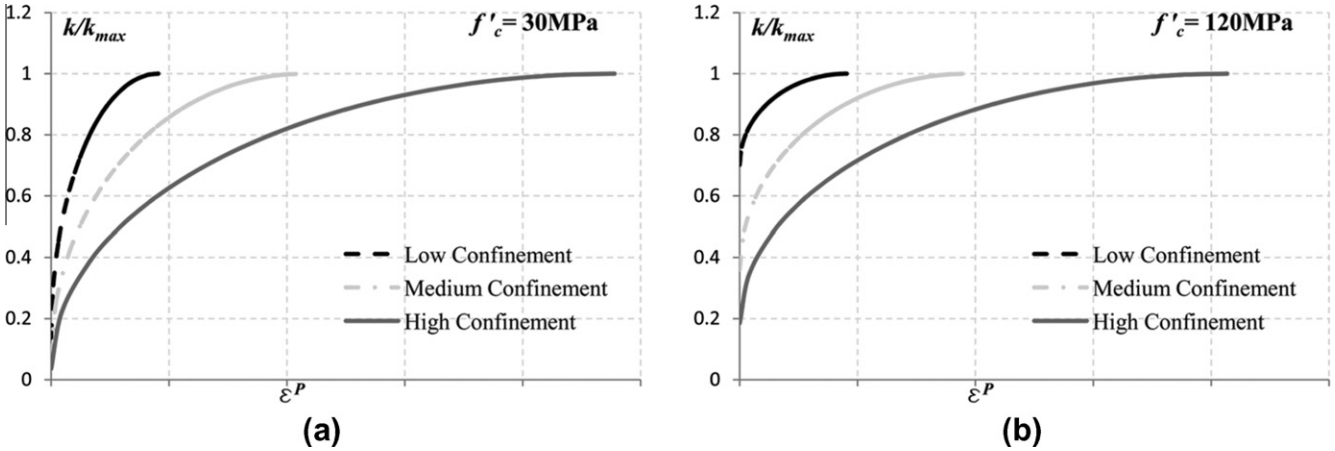


**Fig. 12.** Evolution of the hardening parameter in terms of the plastic strains (a) NSC and (b) HSC.

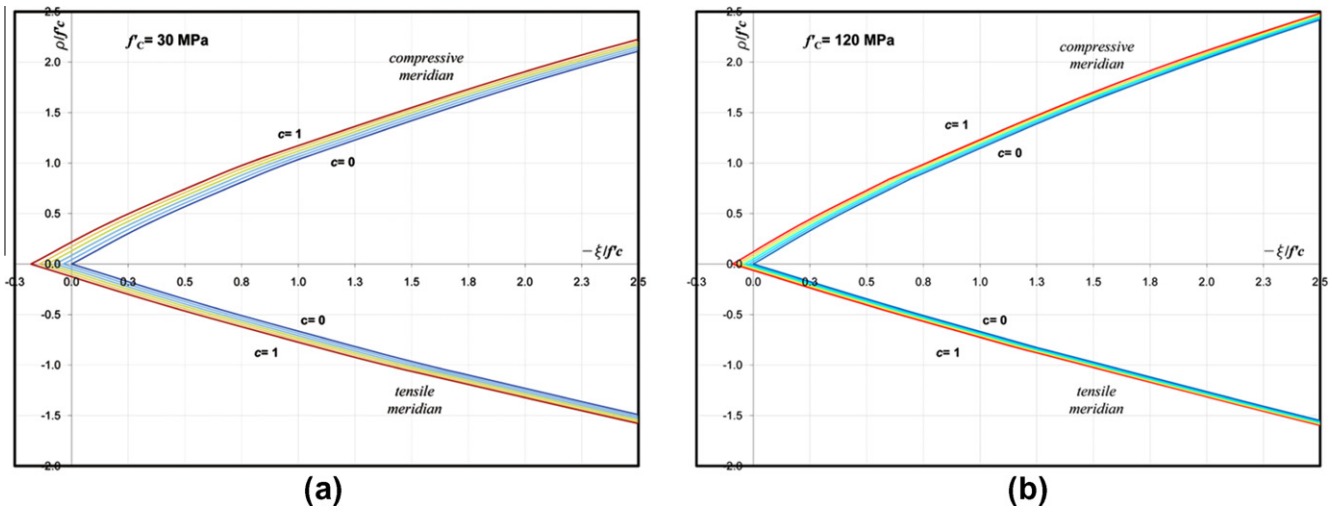


**Fig. 14.** Post peak unloading surfaces (a) NSC and (b) HSC.

processes can be expected. This is capture very efficiently in the models for NSC by Etse and Willam (1994) and Kang and Willam (1999).

### 6.2. Fracture energy based softening law

It is well known that softening is a structural phenomenon rather than a material property, see a.o. Bazănt and Oh (1983), Oliver (1989), van Mier (1997) and Bazănt (2000). If the strength degradation during softening is described within the theoretical framework of the smeared crack approach and using local stress–strain relations, mesh dependent solutions will be obtained. Two different approaches have been considered to avoid this problem: enhanced local theories (Etse and Willam, 1994; Kang and Willam, 1999, etc.), and non-local theories (Etse and Carosio, 2002; Vrech and Etse, 2009, etc.).

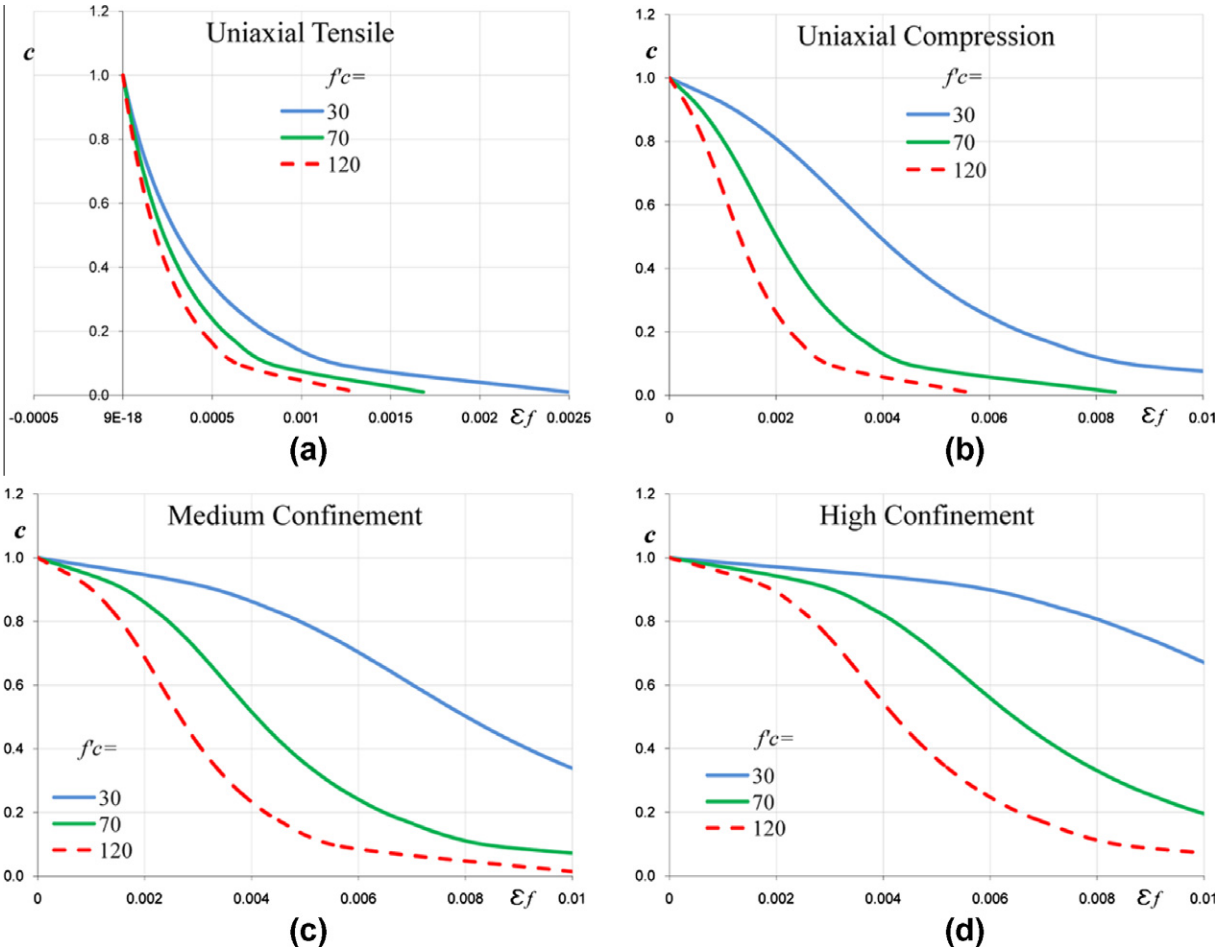


**Fig. 15.** Evolution of decohesion parameter *c* during softening process for different concrete qualities (a) UT (uniaxial tensile); (b) UC (uniaxial compression); (c) medium confinement and (d) high confinement.

In the constitutive formulation presented in this paper, the first approach is adopted. The enrichment of the local constitutive theory is based on fracture energy concepts. For this purpose, the fracture energy $G_f^{\mathrm{I}}$ dissipated during the crack opening process along the surface of the crack $A_t$ in a direct tensile test, is considered to be equal to the energy $W$ dissipated during plastic softening in an equivalent elastoplastic continuum

$$\begin{cases} dG_f^{\mathrm{I}} A_t = \int_{A_t} \boldsymbol{\sigma}_t du_f dA \\ dW_f = \int_{V_t} \boldsymbol{\sigma}_t d\tilde{\varepsilon}_f dV \end{cases} \tag{37}$$

Consequently, the rate of crack opening displacement $\dot{u}_f$ in the discontinuum of high $l_c$ and the rate of the tensile fracture strains $\dot{\tilde{\varepsilon}}_f$ uniformly distributed in the equivalent continuum are related as

$$\dot{u}_f = l_c \dot{\tilde{\varepsilon}}_f \tag{38}$$

In this case (mode I), the characteristic length $l_c$ represents the crack spacing in a direct tensile test $h_t$. To extended this concept to a general mode II type of failure, then the corresponding fracture energy $G_f^{\mathrm{II}}$ needs to be considered as well as the appropriate characteristic length.

The structural response in terms of load–displacement behavior that obtained with this theory will be mesh-independent. Nevertheless, as this regularization strategy does not suppress the loss of strong ellipticity of the constitutive differential equations of the problem, the localization zone of plastic strains will remain being mesh dependent.

In the constitutive formulation presented herein, the approach above described is adopted, leading to a fracture-energy based plastic softening law. The evolution of the softening parameter $c$ is defined as

$$c = \exp\left(\frac{-\delta \kappa_s}{u_r}\right) \tag{39}$$

where $\kappa_s$ is the fracture energy based softening measure, $u_r$ the maximum crack opening displacement, and $\delta$ is a parameter defining the shape of the decay function (see Appendix A).

The evolution law of the fracture energy based softening measure $\kappa_s$ is defined as

$$\dot{\kappa}_s = \dot{u}_f = l_c \dot{\tilde{\varepsilon}}_f = l_c \| \langle \underline{\underline{\boldsymbol{m}}} \rangle \| \dot{\lambda} \tag{40}$$

where the McCauley operator extracts only the tensile components of the gradient to the plastic potential $\underline{\underline{\boldsymbol{m}}}$. The characteristic length $l_c$ for mode II type of fracture is defined as

$$l_c = h_t / \omega_{(G_f^{\mathrm{II}}/G_f^{\mathrm{I}})} \tag{41}$$

In the previous equation, $\omega$ is a parameter that estimates the ratio between the fracture energies in modes II and I ($G_f^{\mathrm{II}}$ and $G_f^{\mathrm{I}}$). It is

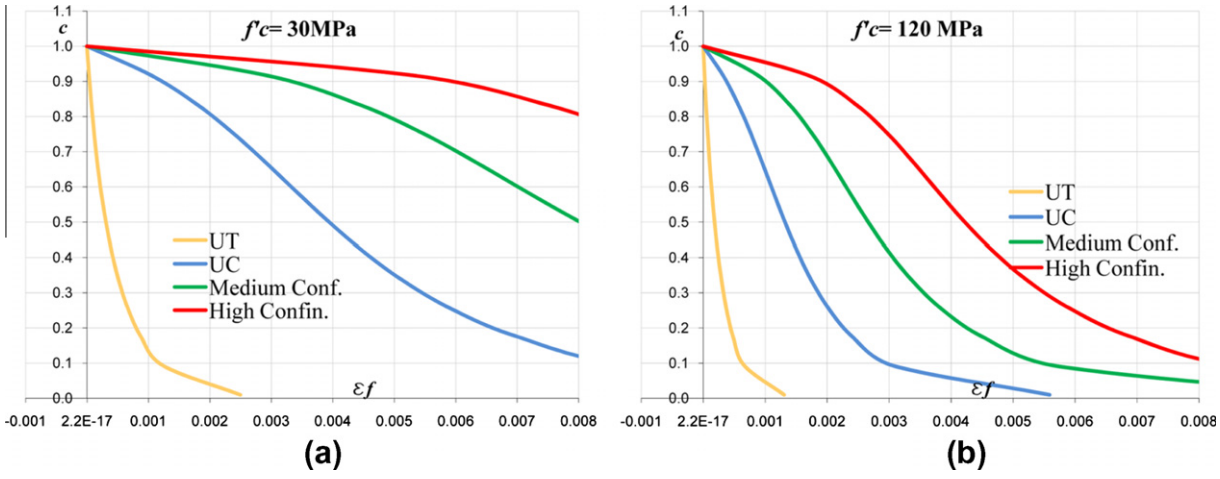


**Fig. 16.** Evolution of decohesion parameter $c$ during softening process for different loading scenarios (a) NSC and (b) HSC.

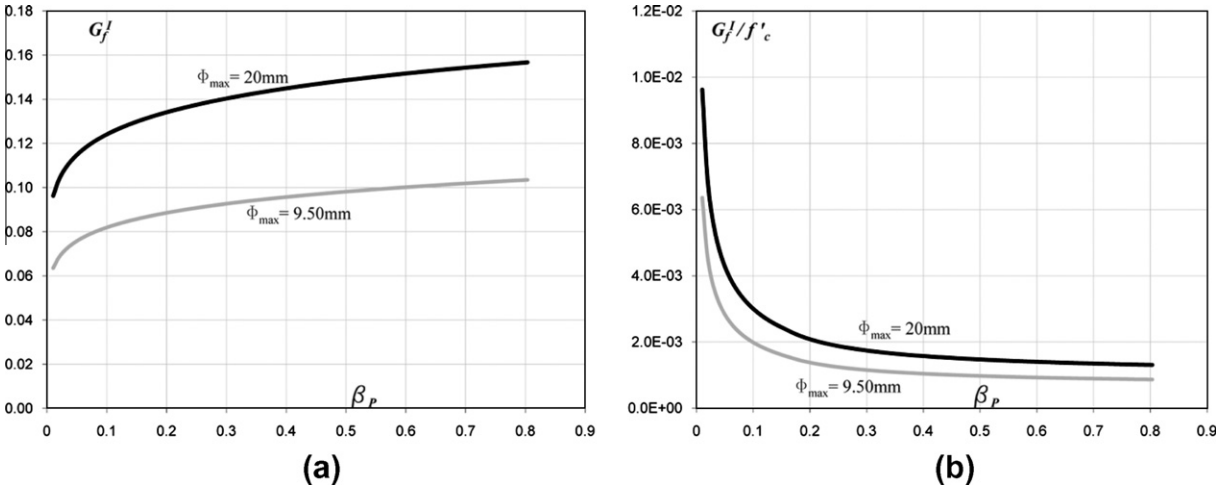


**Fig. 17.** Fracture energy in mode I vs. the performance parameter (a) non normalized and (b) normalized by $f'_c$.

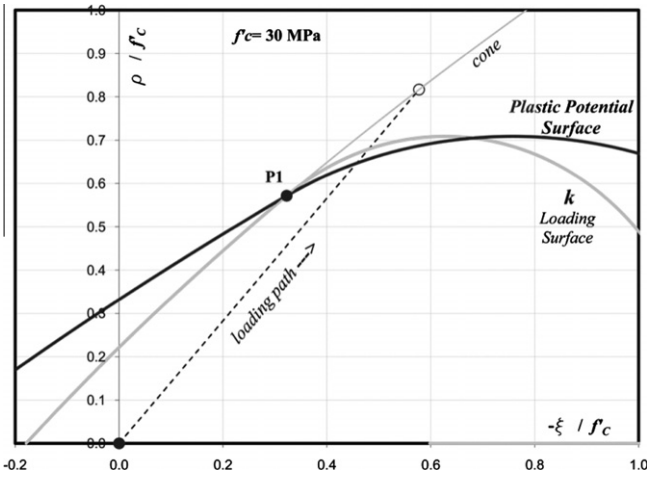


**Fig. 18.** Meridian view of yield surface and plastic potential in hardening regime.

defined in terms of the acting confinement that is represented by the normalized first Haigh Westergaard stress coordinate $\bar{\bar{\xi}}$

$$\omega_{(G_f^{II}/G_f^{I})} = \left[1 + a_{s1}(\bar{\bar{\xi}} - \bar{\bar{\xi}}_t)^3 + a_{s2}(\bar{\bar{\xi}} - \bar{\bar{\xi}}_t)^2 + a_{s3}(\bar{\bar{\xi}} - \bar{\bar{\xi}}_t)\right] \tag{42}$$

thereby $a_{si}$ are calibration functions depending on the material quality, and $\bar{\bar{\xi}}_t$ is the normalized first Haigh Westergaard stress coordinated corresponding to the peak strength of the uniaxial tensile test.

Fig. 15 shows the adopted decohesion function for four different stress histories: uniaxial tensile, uniaxial compression, medium confinement and high confinement.

It may be observed in this figure the incidence of the concrete quality. In all cases, a steeper slope (more brittle behavior) is considered the case of HSC. Note that with increasing confinement the resulting behavior is more ductile.

In Fig. 16 the plots for the four different stress histories considered in Fig. 15 are now organized by concrete quality. Contrarily to HSC, NSC practically do not develop softening behavior under high confinement.

As can be observed in Eq. (39) the controlling parameter in the evolution of concrete strength capacity in softening is the fracture energy in mode I, $G_f^{I}$. In present proposal this is considered to be defined in terms of both the maximum coarse aggregate size $\Phi_{max}$ and the performance parameter $\beta_P$ as

$$G_f^{I}[\mathrm{N/mm}] = g_1\left(\Phi_{max}[\mathrm{mm}]\beta_P^{0.20}\right)^{g_2} \tag{43}$$

where $g_i$ are internal model parameters (see Appendix A).

Fig. 17 (a) shows the dependence of $G_f^{I}$ on the concrete quality parameter $\beta_P$ for two different maximum aggregate sizes. The fracture energy increases with the involved concrete quality, similarly to the increment experimentally signalized by $f_t'$ with concrete quality. In Fig. 17 (b) it is illustrated that the normalized parameter $G_f^{I}/f_c'$ drastically decreases with the involved concrete quality. This is supported by extensive experimental data (see e.g. van Mier, 1997).

## 7. Concrete volumetric behavior and non associated flow rule

Volumetric behavior of concrete in the low confinement regime is characterized by relevant dilations at peak and, particularly, post peak response, see a.o. Shah and Chandra (1968), Smith et al. (1989), Pantazopoulou (1995), and Sfer et al. (2002).

As shown by Shah and Chandra (1968) concrete dilatancy increases with the volume content of coarse aggregate. This conclusion referred only to NSC. Although the experimental evidence on HSC volumetric behavior is limited or inexistent, volumetric expansion can be also expected in case of HSC, when it is subjected to compression in the low confinement regime. However, and due to its superior homogeneity, these expansions or dilatancies are expected to be lower than in case of HSC.

In the framework of the flow theory of plasticity, plastic deformations are controlled by the flow rule. As demonstrated by different researchers, see a.o. Smith et al. (1989) and Etse and Willam (1994), the normality condition leads to strong overestimations of concrete dilatancy. On the other hand, for associated flow, once the failure envelope is reached the stress path keeps increasing until a point is reached where the total strain increment is equal and coaxial with the plastic strain increment. This fictitious stabilizing effect is in contrast with the destabilizing tendencies of the non-associated flow rule. In fact, the non-associated flow brings

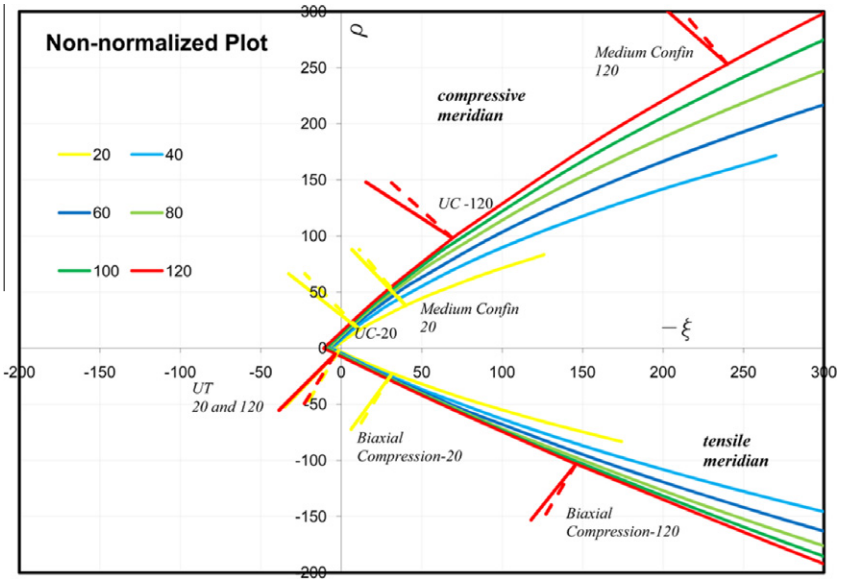


**Fig. 19.** Gradients directions to the yield surface and plastic potential for different concrete qualities and confinement levels.

**Table 1**
List of optional input data in the PDM.

| Optional material parameter | Identification | Default value |
|---|---|---|
| Water/binder ratio | $w/b$ | $w/b$ corresponding to the mean $\beta_P$ from Eq. (2) and (3) |
| Maximum coarse aggregate size | $\Phi_{max}$ | 2 cm |
| Fracture energy in mode I | $G_f^I$ | By Eq. (43) |
| Maximum crack opening displacement in mode I | $u_{rt}$ | 0.02 cm |
| Displacement in mode I | | |
| Crack spacing in a direct tensile test | $h_t$ | 10 cm |
| Uniaxial strength ratio | $\alpha_t = f_t'/f_c'$ | By Eq. (53) |
| Biaxial strength ratio | $\alpha_b = f_b'/f_c'$ | By Eq. (54) |
| Equivalent friction parameter | $m$ | By Eq. (55) |

the stress path down the failure envelope along the low confinement regime and into the tension region. This destabilization signalized by non-associated flow is supported by the experimental evidence on NSC as indicated above.

In the context of the proposed model for concrete of arbitrary strength properties a restricted non-associated flow rule is adopted, whereby the volumetric flow is the only one that does not follow the normality condition.

The plastic potential in hardening and softening, $g_h$ and $g_s$, respectively, are defined as follows

$$g_{h(k)}\begin{cases} g_{h(k)}^{cone} = Ar^2\bar{\rho}^2 + B_c r\bar{\rho} + \eta_{o(\bar{\xi})}C\left(\bar{\xi} - \bar{\xi}_{1(k)}\right) + C\bar{\xi}_{1(k)} - 1 = 0 \\ \quad \text{if } \bar{\xi} \geqslant \bar{\xi}_{1(k)} \\ g_{h(k)}^{cap} = \frac{[\eta_{o(\bar{\xi})}(\bar{\xi}-\bar{\xi}_{1(k)})+(\bar{\xi}_{1(k)}-\bar{\xi}_{cen(k)})]^2}{a_{(k)}^2} + \frac{r^2\bar{\rho}^2}{b_{(k)}^2} - 1 = 0 \\ \quad \text{if } \bar{\xi} < \bar{\xi}_{1(k)} \end{cases} \tag{44}$$

$$g_{s(c)} = Ar^2\bar{\rho}^2 + B_c r\bar{\rho} + \eta_{o(\bar{\xi})}C\left(\bar{\xi} - \bar{\xi}_1\right) + C\bar{\xi}_1 - c = 0 \tag{45}$$

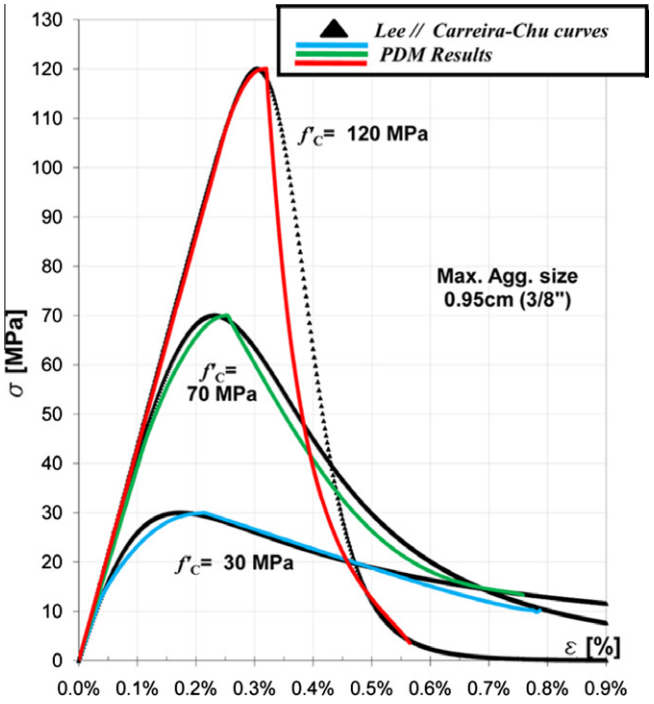


**Fig. 20.** Uniaxial compression-curves proposed by Lee (2002) (HSC), Carreira and Chu (1985) (NSC), and PDM results.

being $\eta_o$ the volumetric non-associativity parameter defined in terms of the normalized first stress coordinate as

$$\eta_o = t_1 \exp\left(t_2 x^{t3}\right) + t_4 \tag{46}$$

with $t_i$ internal model parameters (see Appendix A) and

$$x = \begin{cases} \bar{\xi}_{vertex} - \bar{\xi} & \text{if } \bar{\xi} \leqslant \bar{\xi}_t \\ \bar{\xi}_{vertex} - \bar{\xi}_t & \text{if } \bar{\xi} > \bar{\xi}_t \end{cases} \tag{47}$$

In Fig. 18 can be observed the loading and plastic potential surfaces for a given hardening parameter. The gradient directions to the meridian views of the yield and plastic potential surfaces in hardening regime up to the maximum strength surface are illustrated in Fig. 19. Two different concrete qualities are considered. As can be observed, the level of non-associativity considered in this model increases with the concrete quality while reduces with the confinement pressure.

The non-associated flow in the cone zone of the softening regime as defined by Eq. (45), also depends on the volumetric non-associativity parameter.

## 8. Numerical analysis

The numerical approach for the stress integration $\Delta\underline{\underline{\boldsymbol{\sigma}}} = \Delta\underline{\underline{\boldsymbol{\sigma}}}(\Delta\underline{\underline{\boldsymbol{\varepsilon}}})$ of the Performance Dependent Model is based on the Backward Euler algorithm. A direct method was applied that leads to a single iteration process, while full consistency condition was used for the determination of the plastic multiplier. The consistent tangent operator was obtained and used in the numerical approach.

The following special provisions were considered for the implementation of the Backward Euler algorithm in the transition between cone and cap surfaces:

(i) If the cone portion of the maximum surface is activated, then only softening process may occur during monotonic loading or elastic discharge. Thus, the cap surfaces are not activated.
(ii) Following the proposal by Dolarevic and Ibrahimbegovic (2007), it is considered that trial stresses characterized by first invariants that are equal or larger than the first invariant of the transition point (P1 stress point) are considered to activate the cone portion of the maximum surface. Then, the process described in (i) takes place.
(iii) In case condition (ii) is not fulfilled, then it is considered that the trial stress activates hardening behavior and the Backward Euler projection process to a cap surface related to a larger hardening parameter k is initiated.

**Table 2**
Some calibration values for a medium $\beta_P$.

| $W_p^t$ (MPa) | | | | | |
|---|---|---|---|---|---|
| $f_c'$ | | $\bar{\xi}_{P1}$ | $\bar{\xi}_{f_c'}$ | $\bar{\xi} = -1.00$ | $\bar{\xi} = -4.00$ |
| 30 | | 0.000 | 0.041 | 0.470 | 12.026 |
| 70 | | 0.000 | 0.054 | 0.229 | 5.052 |
| 120 | | 0.000 | 0.053 | 0.188 | 1.898 |
| $l_c$ (cm) | | | | | |
| $f_c'$ | $\bar{\xi} \geqslant \bar{\xi}_{f_t'}$ | $\bar{\xi} = 0.00$ | $\bar{\xi}_{f_c'}$ | $\bar{\xi} = -1.00$ | $\bar{\xi} = -4.00$ |
| 30 | 10.000 | 6.910 | 1.548 | 0.947 | 0.823 |
| 70 | 10.000 | 8.286 | 2.013 | 1.240 | 1.028 |
| 120 | 10.000 | 8.762 | 2.336 | 1.455 | 1.193 |
| $\eta_o$ (−) | | | | | |
| $f_c'$ | | $\bar{\xi}_{Vertex}$ | $\bar{\xi}_{f_c'}$ | $\bar{\xi} = -1.00$ | $\bar{\xi} = -4.00$ |
| 30 | | 0.483 | 0.616 | 0.648 | 0.743 |
| 70 | | 0.456 | 0.560 | 0.582 | 0.643 |
| 120 | | 0.314 | 0.403 | 0.421 | 0.470 |

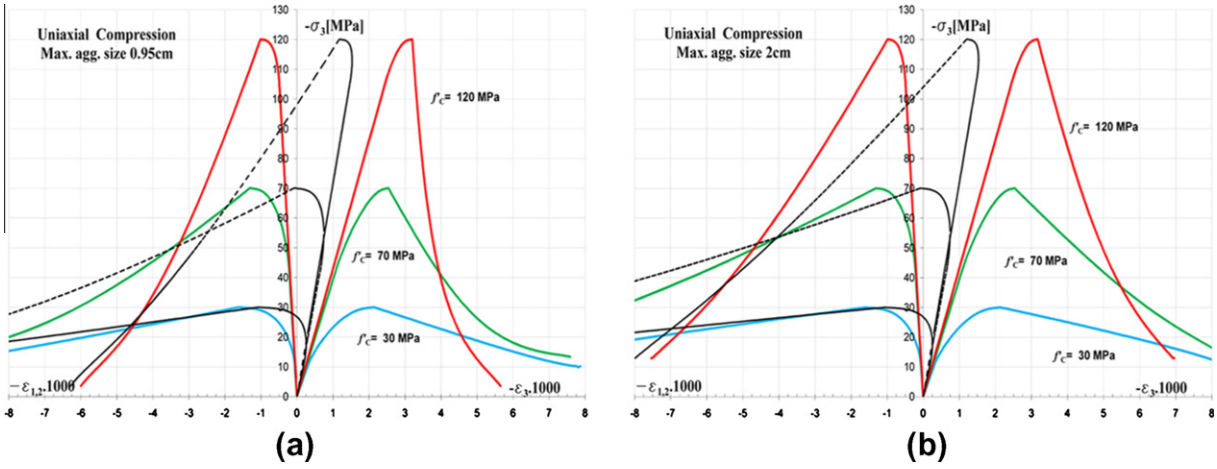


**Fig. 21.** Uniaxial compression PDM results for different concretes and different maximum aggregate sizes $\Phi_{max}$: (a) $\Phi_{max}$ = 0.95 cm; (b) $\Phi_{max}$ = 2.00 cm.

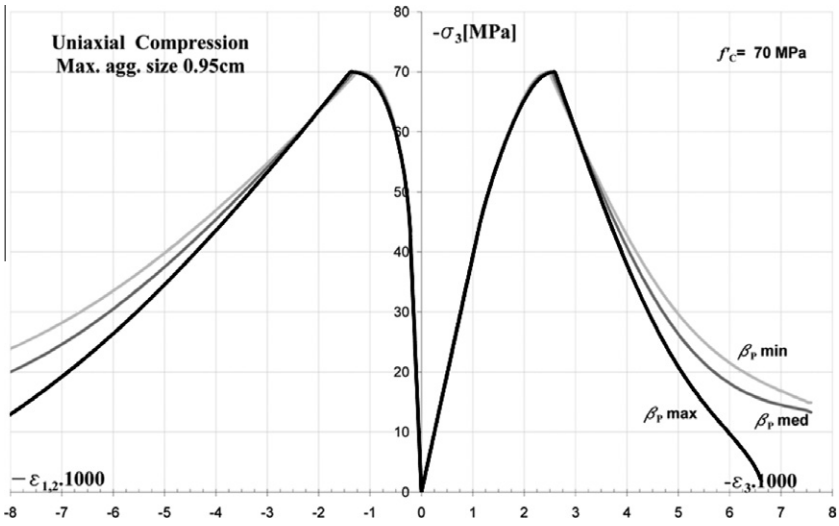


**Fig. 22.** Uniaxial compression PDM results for $\Phi_{max}$ = 0.95 cm and three different $\beta_P$.

(iv) If during the hardening process it is obtained a hardening parameter $k > k_{max}$, then the cone is also activated during this loading step and the softening process is initiated.

The particular features, robustness and efficiency of the numerical approach for the Performance Dependent Model will be addressed in a separated paper.

### 8.1. Input data

Input data of the PDM include both mandatory and optional material parameters. In case one of the optional material parameter is not defined, it is evaluated by specific internal functions.

The mandatory data are: the uniaxial compressive strength $f'_c$, the Young's Modulus $E$ in compression and the Poisson's ratio $\nu$.

The optional material parameters are indicated in Table 1.

Note that the total work hardening parameter $W_t^p$, the internal characteristic length $l_c$, and the degree of non-associativity $\eta_o$ are not considered input variables: they are determined by Eqs. (35), (41) and (46).

The material parameters $\alpha_t$, $\alpha_b$, and $m$, define the cap shape by means of Eqs. (48)–(51). The failure criterion eccentricity imposes a coupling constrain to parameters $\alpha_t$, $\alpha_b$, and $m$, as they should lead to coefficients $B_c$ and $B_t$ satisfying $0.50 \leqslant B_c/B_t \leqslant 1.00$. Internal functions were defined by the authors for these parameters (see Folino et al., 2009; Folino and Etse, 2011), based on a large spectrum of experimental data in the literature. They are useful as in most of the cases the available data are not enough for their appropriate evaluation. The internal functions for these parameters in the PDM are given in Appendix A (see Eqs. (53)–(55)).

**Table 3**
Input data considered for the uniaxial and triaxial compression verification tests.

| Data set | Compr. strength $f'_c$ (MPa) | Young's modulus $E$ (MPa) | Poisson's ratio $\nu$ | Water/binder ratio $w/b$ | Maximum agg. size $\Phi_{max}$ (cm) | Equivalent friction $m$ |
|---|---|---|---|---|---|---|
| Lu (2005) | | | | | | |
| $f'_c = 70$ MPa | 68.6 | 36,000 | 0.20 | 0.327 | 0.95 | 0.91 |
| Xie et al. (1995) | | | | | | |
| $f'_c = 120$ MPa | 119.0 | 28,000 | 0.20 | 0.194 | 1.40 | 1.00 |

### 8.2. Model calibration

The calibration procedure of the PDM required the consideration of experimental results corresponding to concretes of different qualities. Model setup was done by defining appropriate functions for the total work hardening parameter $W_t^P$, the internal characteristic length $l_c$, and the degree of volumetric non-associativity $\eta_o$, in terms of the concrete quality and of the actual first stresses invariant. This was done as explained on what follows.

To calibrate hardening initiation and axial strain levels at peak and residual stresses of uniaxial compression tests, the experimental results by Carreira and Chu (1985) for NSC, and by Lee (2002) for HSC (with silica fume and a maximum coarse aggregate size of 0.95 cm) were considered.

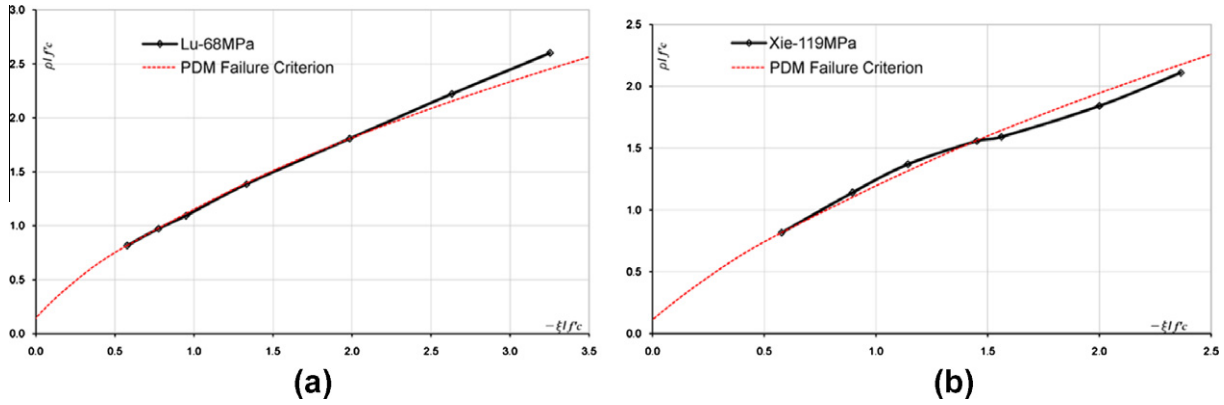


**Fig. 23.** Maximum strength data and PDFC compressive meridian (a) Lu (2005) data; (b) Xie et al. (1995) data.

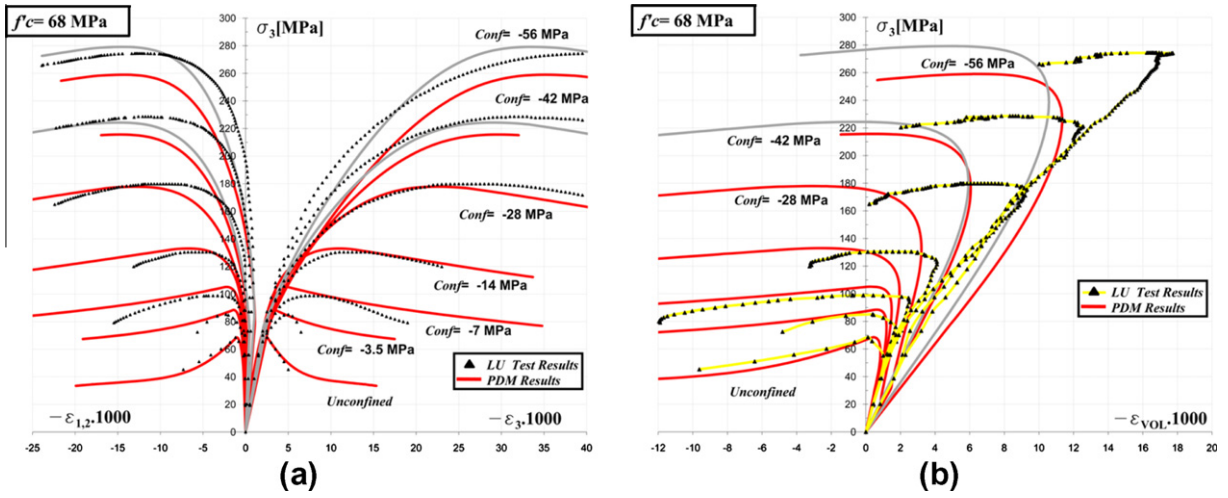


**Fig. 24.** Triaxial compression PDM results vs. Lu (2005) data (a) axial and lateral results; (b) volumetric strains evolution.

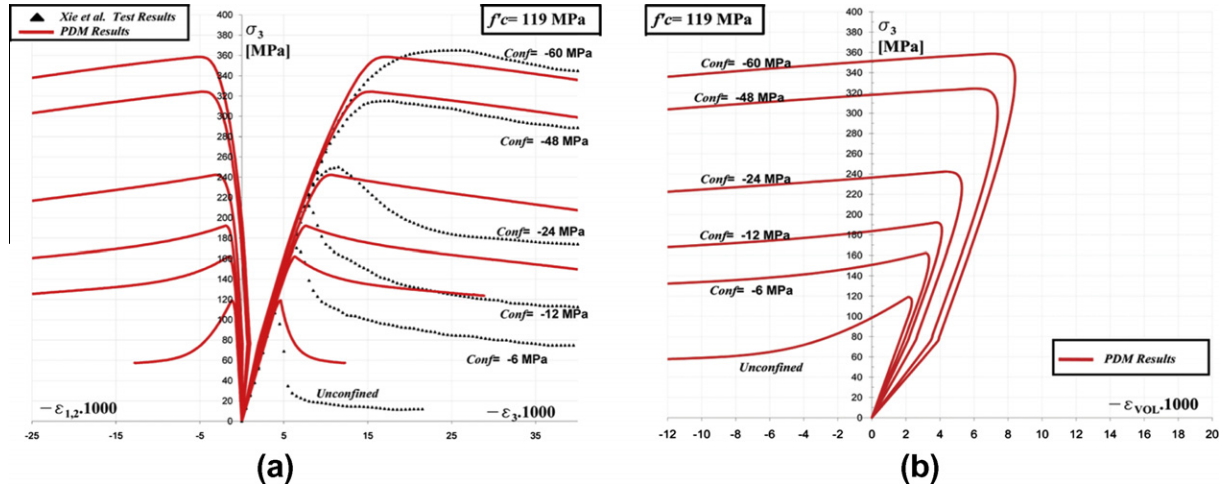


**Fig. 25.** Triaxial compression PDM results vs. Xie et al. (1995) data (a) axial and lateral results; (b) volumetric strains evolution.

In Fig. 20 it may be observed the comparison between PDM predictions and the characteristic mechanical behaviors proposed by Carreira and Chu (1985) and by Lee (2002) for concretes of different strength properties. To calibrate pre a post-peak behaviors of NSC and HSC, a large set of experimental tests were considered. This includes: Ansari and Li (1998), Candappa et al. (2001), Chern et al. (1992), Hampel (2006), Hurlbut (1985), Hussein and Marzouk (2000), Kupfer et al. (1969), Imran and Pantazopoulou (1996), Lim and Nawy (2005), Lu (2005), Ren et al. (2008), Sfer et al. (2002), van Geel (1998) and Xie et al. (1995). The available experimental data, particularly regarding HSC, is scarce and based on very different experimental setups. Nevertheless, they allowed to define internal functions for $W_t^P$, $l_c$, and $\eta_o$, in terms of the concrete quality and of the acting confining pressure, as indicated in Eqs. (35), (41) and (46).

Table 2 shows $W_t^P$, $l_c$, and $\eta_o$ as predicted by the corresponding internal functions in the PDM for different concrete qualities and confinement levels. They are evaluated considering the mean value of $\beta_P$, $h_t$ = 10 cm, and a maximum coarse aggregate size of 2 cm. As can be observed the characteristic length $l_c$ equals $h_t$ when $\bar{\xi} > \bar{\xi}_{f_t'}$, while it approximates the maximum aggregate size in the confinement level corresponding to the uniaxial compression test ($\bar{\xi} = \bar{\xi}_{f_t'}$).

Fig. 21 shows PDM predictions of uniaxial compression tests for different concrete qualities and two different maximum aggregate sizes. The plot includes axial, lateral and volumetric strain evolutions. These results clearly demonstrate the capabilities of the proposed model to capture the relevant improvement of the material strength in uniaxial compression conditions, with the involved quality, as well as the improvement of the ductility in pre and post-peak regimes. The results also show that the constitutive theory is able to reproduce the sensitivity of concrete volumetric behavior to the maximum aggregate size, both in NSC and HSC.

Fig. 22 shows the influence of $\beta_P$ on the axial and lateral strains when the same concrete strength is considered in all different cases. These results demonstrate that concrete quality, as it is considered in the PDM, exceeds $f_c'$ and involve other material features that are taken into account by means of performance parameter $\beta_P$.

**Table 4**
Input data considered for the uniaxial tensile verification tests.

| Data set | Compr. strength $f_c'$ (MPa) | Tensile strength $f_t'$ (MPa) | Young's modulus $E$ (MPa) | Poisson's ratio $v$ | Water/binder ratio $w/b$ | Maximum agg. size $\Phi_{max}$ (cm) |
|---|---|---|---|---|---|---|
| Navalurkar (1996) | | | | | | |
| $f_c' = 45$ MPa | 45.3 | 3.03 | 18,230 | 0.20 | 0.450 | 0.95 |
| $f_c' = 63$ MPa | 62.8 | 3.59 | 21,787 | 0.20 | 0.297 | 0.95 |
| $f_c' = 80$ MPa | 80.0 | 4.47 | 35,625 | 0.20 | 0.234 | 0.95 |
| Li and Ansari (2000) | | | | | | |
| $f_c' = 47$ MPa | 47.2 | 3.10 | 40,679 | 0.20 | 0.460 | 0.95 |
| $f_c' = 86$ MPa | 85.8 | 4.70 | 63,087 | 0.20 | 0.300 | 0.95 |
| $f_c' = 107$ MPa | 107.3 | 5.63 | 64,401 | 0.20 | 0.210 | 0.95 |

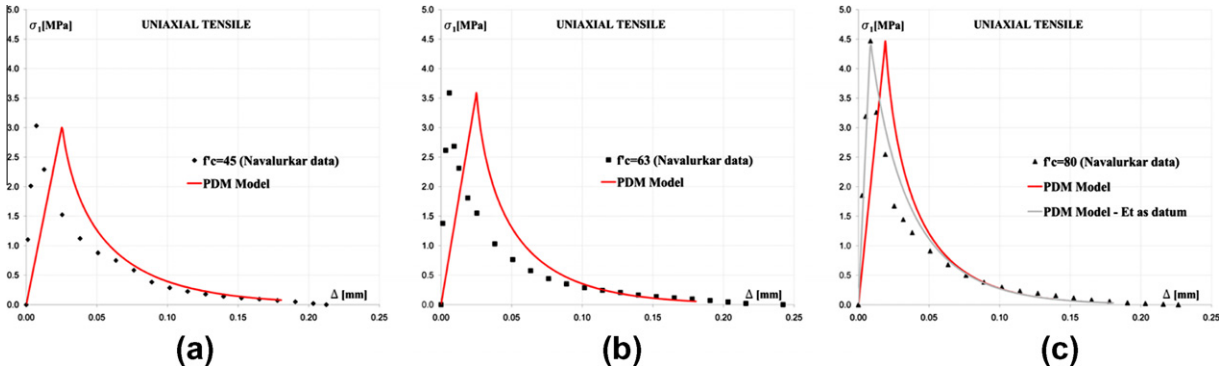


**Fig. 26.** Uniaxial tensile PDM results vs. Navalurkar (1996) data (a) $f_c' = 45$ MPa; (b) $f_c' = 63$ MPa; (c) $f_c' = 80$ MPa.

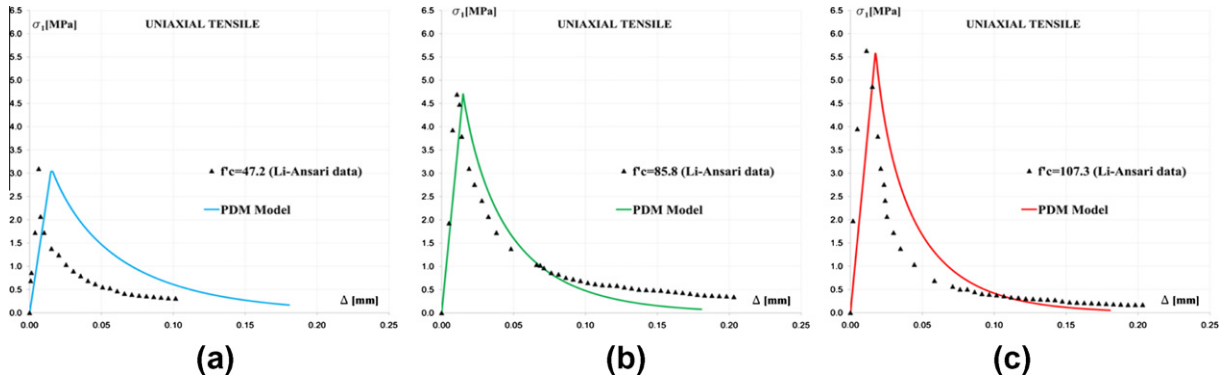


**Fig. 27.** Uniaxial tensile PDM results vs. Li and Ansari (2000) data (a) $f_c' = 47$ MPa; (b) $f_c' = 86$ MPa; (c) $f_c' = 107$ MPa.

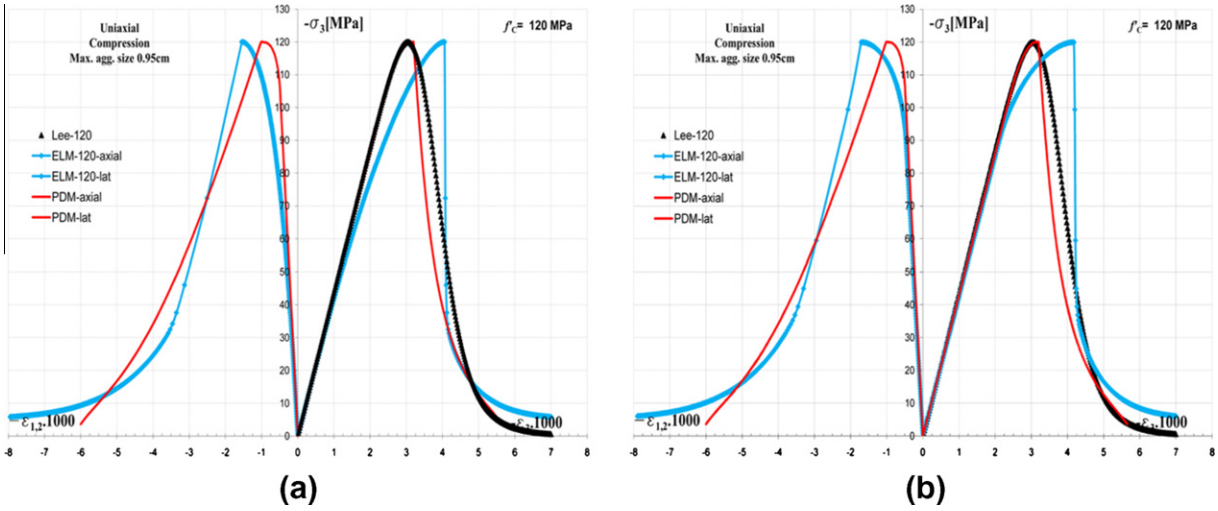


**Fig. 28.** Uniaxial compression, $f_c' = 120$ MPa – Extended Leon Model predictions vs. Lee (2002) and PDM predictions; (a) $k_o = 0.10$; $k_o = 0.75$.

### 8.3. Verification tests

#### 8.3.1. Uniaxial and triaxial compression

For the verification purpose of the PDM predictive capabilities in case of uniaxial and triaxial compression tests, two sets of experimental data were considered. On the one hand, the experiments by Lu (2005), corresponding to a medium strength concrete with $f_c' = 70$ MPa. On the other hand the tests by Xie et al. (1995), that correspond to high strength concrete of $f_c' = 120$ MPa. Unfortunately, the last ones do not include lateral strains. The input data considered in these numerical analyses are summarized in Table 3. They were obtained from the corresponding literature, with exception of $m$ that was determined in terms of the peak strengths for different confinements, as it may seen in Fig. 23.

In Figs. 24 and 25 the plots present the PDM predictions (in continuous lines without markers) vs. the experimental data for different confinement levels. In both cases, the figure on the left hand side shows the axial stress vs. axial and lateral strains, and the one on the right hand side, the axial stress vs. volumetric strains. It may be observed that the model is able to capture the different behaviors of concretes of different qualities. The best accuracy is obtained in uniaxial compression and triaxial compression under medium confinement. In these figures, it may be also observed the relevant importance of the adopted failure surface on the numerical predictions.

#### 8.3.2. Uniaxial tensile

For the verification of the PDM prediction capabilities in the uniaxial tensile test, the experimental data by Navalurkar (1996) corresponding to $f_c' = 45$, 63 and 80 MPa, and the ones by Li and Ansari (2000) corresponding to $f_c' = 47$, 86 and 107 MPa are considered. The input parameters used in these numerical tests are summarized in Table 4. The characteristic length $h_t = 10$ cm was considered. Figs. 26 and 27 compare the numerical predictions with the experimental data. They show very good agreement, with higher accuracy in case of the HSC. As the Young modulus considered in these numerical analysis were the ones given by the authors of the experimental tests for the uniaxial compression tests, the corresponding model predictions do not correctly capture the elastic stiffness in tensile tests and, moreover, the peak stress. This is due to the well-known discrepancy between the elastic stiffness in compression and tension tests. In Fig. 26(c) are depicted (gray line) the model predictions of uniaxial tensile tests when the Young's modulus extracted from the experimental data for these particular tensile tests are considered instead of those corresponding to uniaxial compression. The results show better agreement with the experimental ones. Although so far, there is no final agreement regarding the causes for the differences between the Young modulus in compression and tension, see Gopalaratnam and Shah (1985) and Li and Ansari (2000), they could be supported by the different failure mechanisms of concrete in compression and traction. In compression, concrete failure is initiated by microcracks parallel to the main loading direction, due to secondary tensile stresses in this direction, that follow from the redistribution of the main compressive stresses. Contrarily, concrete failure in uniaxial tensile condition is a direct mechanics with microcracks perpendicular to the main tensile stress. No stress redistribution is required.

The numerical results with the PDM included in Figs. 26 and 27 demonstrate that the gap between Young modula in compression and tension seems to be more significant in case of NSC. This is due to the larger heterogeneity of NSC as compared to HSC.

#### 8.3.3. Extended Leon Model

Finally, the PDM predictions are contrasted against the ones obtained with the Extended Leon Model (ELM) by Etse (1992). The objective is to compare failure predictions of concretes with different strength properties obtained with a sensitive constitutive theory of material quality, such as the PDM, with those obtained with a well-know but quality insensitive material model, such as the ELM. Fig. 28(a) and (b) compare PDM and ELM predictions with experimental results of uniaxial compression tests on $f_c' = 40$MPa and $f_c' = 120$ MPa concretes. As can be observed, both numerical results for NSC concur very well with the experimental ones. However, PDM predictions are more accurate than those of the ELM for the case of the HSC (120 MPa), independently of the initial hardening parameter considered in this last model ($k_o = 0.10$ or $k_o = 0.75$). These results demonstrate the important role of concrete quality in the formulation of the constitutive theory.

## 9. Conclusions

In this paper, a new constitutive formulation for concretes of arbitrary strength properties is proposed. The so-called Performance Dependent Model (PDM) covers the entire spectrum from normal to high strength concretes, with uniaxial compressive strengths ($f_c'$) in the range 20 to 120 MPa.

The PDM is based on the flow theory of plasticity. Its maximum strength criterion is formulated in terms of the performance param-

eter to accurately reproduce the dramatic and non uniform variations of the strength properties in both tensile and compressive meridians, with the involved concrete quality. The performance parameter, previously proposed by the authors, see Folino et al. (2009) and Folino and Etse (2011), takes into account in a realistic and accurate form the influence of the concrete mixture on the concrete strength properties.

The proposed model considers a non uniform hardening law and an isotropic softening rule. They are also defined in terms of the performance parameter to account for the relevant ductility variation in pre and post-peak regimes with the involved material quality. The formulations in hardening and softening also depend on the confining pressure to more accurately predict the transition from brittle to ductile failure behavior of concrete with the acting confinement. The softening formulation is embedded in fracture mechanics concepts to regularize the energy release predicted by the model during post-peak failure processes. In this sense, the energy release properties under mode I and mode II type of fracture were also formulated in terms of the performance parameter to take into account the influence of concrete quality in these relevant fracture features.

The influence of the concrete quality by means of the performance parameter was also considered in the formulation of the non-associated flow rule that controls the volumetric dilatancy of concrete in the low confinement regime.

The predictive capability of the proposed model was demonstrated in this paper by comparing the model predictions with experimental results corresponding to concretes of different qualities. The models allows realistic predictions of concrete failure processes of quite a different strength properties and qualities.

It should be also noted that the proposed constitutive theory can easily be extended to a multiscale-type formulation based on microscopic calibrations of the performance parameter, which controls the failure criterion, the hardening/ softening rules and the non-associativity.

## Acknowledgments

The authors gratefully acknowledge the partial financial support of this work by the Universidad de Buenos Aires (UBACYT 2010-2012 No. 20020090100139), by CONICET (PIP 112-200801-00707), and by the INTECIN and the Laboratory of Materials and Structures at the FIUBA, Argentina.

## Appendix A

### A.1. Parameters A, $B_c$, $B_t$, and C

Coefficients $A$, $B_c$, $B_t$, and $C$ that appear in the mathematical expressions of the different surfaces involved in the proposed constitutive model (i.e. maximum strength surface (Eq. (24)), loading surfaces (27), softening surfaces (36), and plastic potential (44) and (45)), are defined by the following equations

$$A = -\frac{3}{2}\left\{1 + \frac{(m-\sqrt{2})(1-\alpha_b\alpha_t)(\alpha_b-\alpha_t)}{\alpha_b\alpha_t\left[(m-\sqrt{2})(\alpha_b-\alpha_t)+3m\right]}\right\} \tag{48}$$

$$B_c = \sqrt{3}\left\{\sqrt{2} + \frac{(\sqrt{2}m-1)(1-\alpha_b\alpha_t)(\alpha_b-\alpha_t)}{\alpha_b\alpha_t\left[(m-\sqrt{2})(\alpha_b-\alpha_t)+3m\right]}\right\} \tag{49}$$

$$B_t = \sqrt{\frac{3}{2}}\left\{\frac{1+\alpha_t^2}{\alpha_t} + \frac{\left[(m-\sqrt{2})\alpha_t - m\right](1-\alpha_b\alpha_t)(\alpha_b-\alpha_t)}{\alpha_b\alpha_t\left[(m-\sqrt{2})(\alpha_b-\alpha_t)+3m\right]}\right\} \tag{50}$$

$$C = \sqrt{3}m\frac{(1-\alpha_b\alpha_t)(\alpha_b-\alpha_t)}{\alpha_b\alpha_t\left[(m-\sqrt{2})(\alpha_b-\alpha_t)+3m\right]} \tag{51}$$

The eccentricity $e$ is defined by the following equation

$$e = \frac{-B_t + \sqrt{B_t^2 + 4\cdot A\cdot(1 - C\cdot\bar{\xi})}}{-B_c + \sqrt{B_c^2 + 4\cdot A\cdot(1 - C\cdot\bar{\xi})}} \tag{52}$$

### A.2. Internal functions in the PDFC

$$\alpha_{t(\beta_P f_c')} = \frac{6.70\beta_P^{0.27}}{f_c'[\text{MPa}]} \tag{53}$$

$$\begin{aligned} &\alpha_{b(\beta_P f_c')} = k_b.\alpha_t \\ &k_b = 2.70\left(f_c'[\text{MPa}]\right)^{0.45} \leqslant 20 \end{aligned} \tag{54}$$

$$\begin{aligned} &m_{(\beta_P f_c')} = k_m\beta_P^{0.05} \\ &k_m = \begin{cases} 1.04 + 0.05 f_c'[\text{MPa}]/90 & f_c' < 90\ \text{MPa} \\ 1.09 & f_c' \geqslant 90\ \text{MPa} \end{cases} \end{aligned} \tag{55}$$

### A.3. First loading surface in hardening regime

The first loading surface (see Fig. 11), characterized by the initial hardening parameter $k_o$, defines when the inelastic behavior begins. It is defined by the general equation

$$\frac{x^2}{a_o^2} + \frac{y^2}{b_o^2} = 1 \quad \text{with} \quad x = \bar{\xi} - \bar{\xi}_{ceno}; \quad y = \bar{\rho}_c \tag{56}$$

The unknowns $a_o$, $b_o$ and $x_{ceno}$ are obtained from the following conditions: (a) the ellipse must pass through the point "P1" on the compressive meridian of the failure surface; (b) it is tangent to the failure surface at "P1"; and (c) it must pass through point "P2" of stress coordinates $(\bar{\xi}_2; y_2 = \bar{\rho}_{c2}) = \left(-\alpha_{el}/\sqrt{3}; \alpha_{el}\sqrt{\frac{2}{3}}\right)$.

Coefficient $\alpha_{el}$ is defined such that in a uniaxial compression test plastic strains begin when the compressive stress is equal to $(\alpha_{el}\cdot f_c')$. As it was previously mentioned in the Section 2, in a uniaxial compression test the elastic range in the case of HSC is considerably more extended than the corresponding to NSC. While for NSC the proportional zone is about 30% of $f_c'$, it can reach and overpass 80% of $f_c'$ in the case of HSC. Regarding this, the following expression was adopted for $\alpha_{el}$

$$0.10 \leqslant \alpha_{el} = \beta_P^{0.11} - 0.50 + \frac{f_c'[\text{MPa}]}{300} \leqslant 0.95 \tag{57}$$

The first ellipse parameters end defined as follows

$$x_{ceno} = \frac{(\bar{\xi}_{1o}^2 - \bar{\xi}_{2o}^2)n_1 y_1 - \bar{\xi}_{1o}(y_1^2 - y_2^2)}{2y_1 n_1(\bar{\xi}_{1o} - \bar{\xi}_{2o}) - (y_1^2 - y_2^2)} \tag{58}$$

$$a_o^2 = x_1^2 - \frac{x_1 y_1}{n_1}; \text{ and } b_o^2 = \frac{a_o^2 y_1^2}{(a_o^2 - x_1^2)} \tag{59}$$

$$\text{with } n_1 = \frac{-C}{2Ay_1 + B_c} \tag{60}$$

Finally, to obtain the stress coordinate $y_1 = \bar{\rho}_{c1}$ of "P1", the ellipticity conditions: $a_o^2 > 0$, $b_o^2 > 0$ and $a_o^2/b_o^2 > 0$ are considered together with the condition $\bar{\xi}_1 > \bar{\xi}_2$, leading to

$$y_1^2 + \frac{2}{B_c}\left[Ay_2^2 - 1 + C\bar{\xi}_2\right]y_1 + y_2^2 > 0 \tag{61}$$

The roots of Eq. (61) define maximum and minimum values $y_{1max}$, $y_{1min}$ of the domain of possible stress coordinates $y_1$. Among all possible values in the $y_{1max}$, $y_{1min}$ domain, the following is adopted in present model formulation

$$y_1 = y_{1min} + 0.17(y_{1max} - y_{1min}) \tag{62}$$

From Eq. (26), the hardening parameter corresponding to the first yield surface in pre peak regime is

$$k_o = y_1/\sqrt{2/3} \tag{63}$$

### A.4. The successive hardening elliptical caps on the compressive meridian

As previously mentioned, during the hardening process the contact point "P1" between cap and cone moves along the compressive meridian of the failure criterion towards the increasing confining zone. Thus, new hardening level parameters $k_i = \bar{\rho}_{cP1_i}/\sqrt{2/3}$ are generated. The successive elliptical caps on the compressive meridian are tangent to the failure cone at actual contact point "P1$^i$", while the ratio between the two ellipse semi axes are considered to remain constant $\left(a^2/b^2 = a_o^2/b_o^2 = R_{ab}\right)$. Then

$$\frac{x^2}{a^{i2}} + \frac{y^2}{b^{i2}} = 1 \tag{64}$$

$$\text{with } x = \bar{\xi} - x^i_{cen};\quad y = \overline{\rho_c}$$
$$\text{and } x^i_{cen} = \bar{\xi}^i_1 + n^i_1 R_{ab}\bar{\rho}^i_{c1};\quad a^{i2} = \left(\bar{\xi}^i_1 - x^i_{cen}\right)^2 + R_{ab}\left(\bar{\rho}^i_{c1}\right)^2; b^{i2} = a^{i2}/R_{ab} \tag{65}$$

After replacing in (65) the coordinates of "P1" expressed in terms of the hardening parameter $k$, the ellipses parameters in Eq. (27) take the form

$$\bar{\xi}_{cen(k)} = \frac{1}{C}\left[1 - A\frac{2}{3}k^2 - B_c\sqrt{\frac{2}{3}}k - \sqrt{\frac{2}{3}}\frac{C^2 R_{ab}}{2Ak\sqrt{2/3} + B_c}k\right] \tag{66}$$

$$a^2_{(k)} = \left[\frac{1}{C}\left(1 - \frac{2}{3}Ak^2 - \sqrt{\frac{2}{3}}B_c k\right) - \bar{\xi}_{cen(k)}\right]^2 + \frac{2}{3}R_{ab}k^2 \tag{67}$$

$$b^2_{(k)} = a^2_{(k)}/R_{ab} \tag{68}$$

The final formulation of the actual cap expressed in terms of the three Haigh Westergaard stress coordinates (Eq. (27)) is obtained by extending the equation corresponding to the cap on the compressive meridian (Eq. (64)) to all possible meridians. This can be done by introducing the ellipticity factor $r$ of Eq. (23) in Eq. (64) while extending the fulfillment of condition in Eq. (22) to the cap as

$$\forall 0^0 \leqslant \theta \leqslant 60^0 \Rightarrow \bar{\rho}_c = r\bar{\rho} \tag{69}$$

### A.5. Internal parameters involved in softening law

When fracture energy in mode I $G^I_f$ is not an input datum, it is evaluated by Eq. (43), with parameters $g_1 = 0.03$, and $g_2 = 0.56$, leading to the following expression

$$G^I_f[\text{N/mm}] = 0.03\Phi^{0.56}_{max}\beta^{0.112}_P \text{ with } \Phi_{max} \text{ in [mm]} \tag{70}$$

From Eq. (37) and from the negative exponential function adopted for the tension decay (Eq. (39)), it follows

$$G^I_f = f'_t\int_0^{u_{rt}} e^{\frac{-\bar{\delta}u}{u_{rt}}}du = \frac{-f'_t u_{rt}}{\delta}(e^{-\delta} - 1) \Rightarrow \frac{G^I_f}{f'_t u_{rt}}\delta + e^{-\delta} - 1 = 0 \tag{71}$$

where parameter $u_{rt}$ is the maximum crack opening in a uniaxial tensile test, considered as an optional input datum with a default value of 0.20 mm, and $\delta$ is a coefficient defining the shape of the decay function. The latter is obtained by an approximated solution of Eq. (71) as follows

$$\delta = 0.99495\left(\frac{G^I_f}{f'_t u_{rt}}\right)^{-1.002098} \tag{72}$$

In the expression above, it may be observed that $\delta$ depends on $G^I_f$ and consequently, takes different values for different coarse aggregates.

### A.6. Non associative factor $\eta_o$

The actual calibration of the internal parameters $t_1$, $t_2$, $t_3$, and $t_4$ in Eq. (46) leads to the following expression of the non associative factor $\eta_o$

$$\eta_o = 7.38\alpha_t C\exp(-2.46\alpha_t C x^{-0.48\alpha_t}) - 0.30\beta_P - 0.37$$
$$\text{with } x = \begin{cases} \bar{\xi}_{vertex} - \bar{\xi} & \text{if } \bar{\xi} \leqslant \bar{\xi}_t \\ \bar{\xi}_{vertex} - \bar{\xi}_t & \text{if } \bar{\xi} > \bar{\xi}_t \end{cases} \tag{73}$$

## References


Ansari, Q., Li, Q., 1998. High-strength concrete subjected to triaxial compression. ACI Materials Journal 95 (6), 747–755.

Bazănt, Z., 2000. Size effect. International Journal of Solids and Structures 37, 69–80.

Bazănt, Z., Oh, B.-H., 1983. Crack band theory for fracture of concrete. Materials and Structures (RILEM, Paris) 16, 155–177.

Candappa, D., Sanjayan, J., Setunge, S., 2001. Complete triaxial stress–strain curves of high-strength concrete. ASCE Journal of Materials in Civil Engineering 13 (3), 209–215.

Carreira, D., Chu, K., 1985. Stress–strain relationship for plain concrete in compression. ACI Journal Proceedings 82 (6), 797–804.

Chen, W., Han, D., 1988. Plasticity for Structural Engineers. Springer Verlag, New York, US.

Chern, J., Yang, H., Chen, H., 1992. Behavior of steel fiber reinforced concrete in multiaxial loading. ACI Materials Journal 89 (1), 32–40.

de Borst, R., 1993. A generalisation of J2-flow theory for polar continua. Computer Methods in Applied Mechanics and Engineering 103 (3), 347–362.

de Borst, R., Pamin, J., Peerlings, R., Sluys, L., 1993. On gradient-enhanced damage and plasticity models for failure in quasi-brittle and frictional materials. Computational Mechanics 17 (1–2), 130–141.

Dolarevic, S., Ibrahimbegovic, A., 2007. A modified three-surface elasto-plastic cap model and its numerical implementation. Computers and Structures 85, 419–430.

Dvorkin, E., Cuitiño, A., Gioia, G., 1989. A concrete material model based on non-associated plasticity and fracture. Journal Engineering Computations 6 (4), 281–294.

Etse, G., 1992. Theoretische und numerische untersuchung zum diffusen und lokalisierten Versagen in Beton. Ph.D. Thesis, University of Karlsruhe, Karlsruhe, Germany

Etse, G., Carosio, A., 2002. Diffuse and localized failure predictions of Perzyna viscoplastic models for cohesive frictional materials. Latin American Applied Research 32, 21–31.

Etse, G., Willam, K., 1994. Fracture energy formulation for inelastic behavior of plain concrete. ASCE Journal of Engineering Mechanics 120 (9), 1983–2011.

Etse, G., Nieto, M., Steinmann, P., 2003. A micropolar microplane theory. International Journal of Engineering Science 41 (13–14), 1631–1648.

Folino, P., Etse, G., 2011. Validation of the performance dependent failure criterion for concretes. ACI Materials Journal 108 (3), 261–269.

Folino, P., Etse, G., Will, A., 2009. A performance dependent failure criterion for normal and high strength concretes. ASCE Journal of Engineering Mechanics 135 (12), 1393–1409.

Fossum, A., Fredrich, J., 2000. Cap plasticity models and compactive and dilatant pre-failure deformation. In: Proceedings of the 4th North American Rock Mechanics Symposium, Seattle, WA, July 31–August 3, 2000. A.A. Balkema, Rotterdam, The Netherlands, pp. 1169–1176.

Giaccio, G., Rocco, C., Violini, D., Zappitelli, J., Zerbino, R., 1992. High strength concretes incorporating different coarse aggregates. ACI Materials Journal 89 (3), 242–246.

Giaccio, G., Rocco, C., Zerbino, R., 1993. The fracture energy (Gf) of high-strength concretes. Materials and Structures 26, 381–386.

Gopalaratnam, V., Shah, S., 1985. Softening response of plain concrete in direct tension. ACI Materials Journal 82 (3), 310–323.

Grassl, P., Jirásek, M., 2006. Damage-plastic model for concrete failure. International Journal of Solids and Structures 43, 71667196.

Grassl, P., Lundgren, K., Gylltoft, K., 2002. Concrete in compression: a plasticity theory with a novel hardening law. International Journal of Solids and Structures 39, 52055223.

T. Hampel, Experimental analysis of the behavior of high performance concrete under multiaxial states of stresses. Ph.D. Thesis, Technischen Universität Dresden, Dresden, Germany, 2006.

Han, D., Chen, W., 1987. Constitutive modeling in analysis of concrete structures. ASCE Journal of Engineering Mechanics 113 (4), 577–593.

Hurlbut, B., 1985. Experimental and computational investigation of strain-softening in concrete. Master's Thesis, University of Colorado, Boulder, US.

Hussein, A., Marzouk, H., 2000. Behavior of high-strength concrete under biaxial stresses. ACI Materials Journal 97 (1), 27–36.
Imran, I., Pantazopoulou, S., 1996. Experimental study of plain concrete under triaxial stress. ACI Materials Journal 93 (6), 589–601.
Jason, L., Huerta, A., Pijaudier-Cabot, G., Ghavamian, S., 2006. An elastic plastic damage formulation for concrete: application to elementary tests and comparison with an isotropic damage model. Computer Methods in Applied Mechanics and Engineering 195 (52), 7077–7092.
Kang, H., Willam, K., 1999. Localization characteristics of triaxial concrete model. ASCE Journal of Engineering Mechanics 125 (8), 941–950.
Kupfer, H., Hilsdorf, H., Rusch, H., 1969. Behavior of concrete under biaxial stresses. ACI Journal Proceedings 66 (8), 656–666.
Lee, I., 2002. Complete stress–strain characteristics of high performance concrete. Ph.D. Thesis, New Jersey Institute of Technology, New Jersey, US.
Lee, J., Fenves, G., 1998. Plastic-damage model for cyclic loading of concrete structures. ASCE Journal of Engineering Mechanics 124 (8), 892–900.
Li, Q., Ansari, Q., 1999. Mechanics of damage and constitutive relationships for high-strength concrete in triaxial compression. ASCE Journal of Engineering Mechanics 125 (1), 1–10.
Li, Q., Ansari, Q., 2000. High-strength concrete in uniaxial tension. ACI Materials Journal 97 (1), 49–57.
Lim, D., Nawy, E., 2005. Behavior of plain and steel-fiber-reinforced high strength concrete under uniaxial and biaxial compression. Magazine of Concrete Research 57 (10), 603–610.
Lu, X., 2005. Uniaxial and triaxial behavior of high strength concrete with and without steel fibers. Ph.D. Thesis, New Jersey Institute of Technology, US.
Luccioni, B., Oller, S., Danesi, R., 1996. Coupled plastic-damage model. Computer Methods in Applied Mechanics and Engineering 37, 81–90.
Navalurkar, R., 1996. Fracture mechanics of high strength concrete members. Ph.D. Thesis, New Jersey Institute of Technology, New Jersey, US.
Oliver, J., 1989. A consistent characteristic length for smeared cracking models. International Journal for Numerical Methods in Engineering 28, 461–474.
Oller, S., 1988. Un modelo de daño continuo para materiales friccionales. Ph.D. Thesis, UPC, Barcelona, Spain.
Pantazopoulou, S., 1995. Role of expansion on mechanical behavior of concrete. ASCE Journal of Structural Engineering 121 (12), 1795–1805.
Papanikolaou, V., Kappos, A., 2007. Confinement-sensitive plasticity constitutive model for concrete in triaxial compression. International Journal of Solids and Structures 44 (21), 7021–7048.
Pramono, E., Willam, K., 1989. Implicit integration of composite yield surfaces with corners. Engineering Computations 6, 186–197.
Rashid, M., Mansur, M., Paramasivam, P., 2002. Correlations between mechanical properties of high-strength concrete. Journal of Materials in Civil Engineering 14 (3), 230–238.
Ren, X., Yang, W., Zhou, Y., Li, J., 2008. Behavior of high-performance concrete under uniaxial and biaxial loading. ACI Materials Journal 105 (6), 548–557.
Sfer, D., Carol, I., Gettu, R., Etse, G., 2002. Experimental study of the triaxial behavior of concrete. ASCE Journal of Engineering Mechanics 128 (2), 156–163.
Shah, S., Chandra, S., 1968. Critical stress, volume change, and microcracking of concrete. ACI Journal 65-57, 770–780.
Smith, S., Willam, K., Gerstle, K., Sture, S., 1989. Concrete over the top, or: is there life after peak. ACI Materials Journal 86 (5), 491–497.
van Geel, E., 1998. Concrete behavior in multiaxial compression. Ph.D. Thesis, Technische Universiteit Eindhoven, The Netherlands.
van Mier, J., 1997. Fracture Processes of Concrete. CRC Press, Boca Raton, Florida, US.
Vrech, S., 2007. Simulación computacional de procesos de falla localizada basada en teoría de gradientes. Ph.D. Thesis, Universidad Nacional de Tucumán, Tucumán, Argentina
Vrech, S., Etse, G., 2009. Gradient and fracture energy-based plasticity theory for quasi-brittle materials like concrete. Computer Methods in Applied Mechanics and Engineering 199 (1–4), 136–147.
Willam, K., Warnke, E., 1974. Constitutive model for the triaxial behavior of concrete. In: Intl. Assoc. Bridge Struct. Engrg., Report 19, Section III, Zurich, Switzerland, pp. 1–30.
Xie, J., Elwi, A., Mac Gregor, J., 1995. Mechanical properties of three high-strength concretes containing silica fume. ACI Materials Journal 92 (2), 135–145.